Simulation of ENSO-like Phenomena with a Low-Resolution Coupled GCM of the Global Ocean and Atmosphere

NGAR-CHEUNG LAU, S. G. H. PHILANDER, AND MARY JO NATH

Geophysical Fluid Dynamics Laboratory/NOAA, Princeton University, Princeton, New Jersey

(Manuscript received 22 October 1990, in final form 10 September 1991)

ABSTRACT

A 140-year simulation of the ocean–atmosphere climate system has been performed by the GFDL Climate Dynamics Project using a low-resolution coupled general circulation model (GCM). The model was subjected to annually averaged insolation throughout the integration. This coupled system exhibits well-defined fluctuations in the tropical Pacific, with a preferred time scale of 3–4 years. The characteristics of these recurrent anomalies were examined by applying an extended empirical orthogonal function (EEOF) analysis to selected model variables. These results indicate that the simulated oscillations are accompanied by coherent changes in the atmospheric and oceanic circulation.

The spatial patterns associated with the leading EEOF mode indicate that SST anomalies make their first appearance off the Peru–Ecuador coast and then migrate steadily westward, with an average transit time of 12–15 months. The arrival and eventual decay of SST fluctuations in the western Pacific is typically followed by the initiation of anomalies of the opposite polarity along the American coasts. The space–time evolution of various meteorological and oceanographic signals exhibits well-defined phase relationships with the SST perturbations. Some aspects of the model behavior during these warm and cold episodes are reminiscent of observed phenomena associated with the El Niño–Southern Oscillation (ENSO).

Analysis of the climatological heat budget for the top ocean layer indicates a near balance between horizontal and vertical temperature advection by the time-mean flow, vertical diffusion, and heat input from the overlying atmosphere. Contributions of transient effects to this balance are negligible. The principal mechanisms associated with the simulated ENSO-like cycles were then studied by examining the local heat budget for the SST perturbations. It is shown that the relative importance of various linear advective processes in the heat budget exhibits a notable dependence on geographical location and on the specific phase of the ENSO-like cycle.

1. Introduction

Considerable research efforts have recently been devoted to a better understanding of the variability of the coupled ocean–atmosphere system. Of particular interest is a phenomenon known as the El Niño–Southern Oscillation (ENSO), an irregular, interannual fluctuation between warm and cold conditions in the tropical Pacific Ocean. Bjerknes (1969) first identified unstable interactions between the atmosphere and the tropical Pacific Ocean as the cause of this phenomenon. Attempts to quantify Bjerknes' ideas have followed two complementary routes. One route uses stability analyses to establish the properties of unstable modes: the range of wavelengths and frequencies that are unstable, and the manner in which the evolution of El Niño depends on the processes that influence sea surface temperature (SST) variations (Hirst 1986; Battisti and Hirst 1989). The other route uses coupled ocean–atmosphere models that march forward in time so as to simulate the excitation and development of some of the unstable modes of the ocean–atmosphere system. The latter coupled models typically have an oceanographic component that is capable of reproducing reasonably realistic SST fluctuations in response to forcing with the observed fluxes of momentum and heat across the ocean surface, and an atmospheric component capable of reproducing reasonably realistic surface winds in response to the observed SST field. However, the coupled systems designed by different research groups behave in a surprising variety of ways. Some of these models simulate self-sustaining ENSO events; others do not. For those models that do reproduce a Southern Oscillation with realistic warm El Niño and cold La Niña states, the manner in which ENSO evolves can be very different. Hence, the fidelity of a coupled model cannot be judged on the basis of the performance of each of its components in isolation.

The coupled models developed thus far fall into two groups: anomaly models that specify the time-mean state of the ocean and atmosphere and more comprehensive models that simulate both the mean state and interannual variability. The anomaly models generally

Corresponding author address: Dr. Ngar-Cheung Lau, Princeton University, Geophysical Fluid Dynamics Laboratory/NOAA, Forrestal Campus, US Route 1, P.O. Box 308, Princeton, NJ 08542.

succeed in reproducing ENSO-like phenomena (Anderson and McCreary 1985; Cane and Zebiak 1985; Schopf and Suarez 1988; Battisti 1988). However, considerable difficulties have been encountered by various groups (e.g., Latif et al. 1988; Gordon 1989; Delecluse and Andrich, personal communication, 1990) in their attempts to reproduce realistic ENSO events by using the more comprehensive coupled general circulation models (GCMs). Some progress in the simulation of the Southern Oscillation with a coupled GCM developed at the National Center for Atmospheric Research has recently been reported by Meehl (1990). A comprehensive review of the performance of 17 different coupled GCMs in simulating various facets of tropical air–sea interaction has been offered by Neelin et al. (1992).

Neelin's (1989, 1990) studies offer some insights on the different ways in which the various models behave. He explored how the fate of an initial perturbation depends on the strength of the coupling between the ocean and atmosphere. His analysis indicates that weak coupling leads to damped oscillations, an increase in the strength of the coupling permits self-sustaining interannual oscillations, and very strong coupling results in secondary instabilities and chaotic fluctuations. The factors that control the strength of the coupling between the ocean and atmosphere are poorly understood but are believed to include the mean depth of the thermocline in the equatorial zone, thermal dissipation of the oceanic surface layer, value of the drag coefficient used in computing wind stresses, speed of the mean ocean currents, and oceanic equivalent depth (Zebiak and Cane 1987), as well as the mean zonal SST gradient along the equator (Neelin 1990) and the magnitude of the wind stress forcing (Meehl 1990). The properties of interannual oscillations are very sensitive to small changes in the mean conditions. The models that specify the mean states and that reproduce a Southern Oscillation often need to be tuned carefully. In more comprehensive models, the problem is primarily concerned with the mean state. Some of these models suffer from climate drifts and reach equilibrium states that differ considerably from the observed climate. The mean states attained by the latter models are stable to perturbations, so that self-sustaining interannual oscillations cannot be excited.

During recent years, multiyear simulations of the ocean–atmosphere climate have been performed with two versions of a coupled GCM at the Geophysical Fluid Dynamics Laboratory (GFDL). The same atmospheric component has been used in both versions. This model atmosphere is known to yield a realistic response in the presence of prescribed SST anomalies (see Lau 1985). The oceanic component of the two versions differs mainly in spatial resolution, eddy diffusivity, and model geometry. The low-resolution version (hereafter referred to as LR) has a horizontal resolution of 4.5° latitude and 3.75° longitude. In the upper portion of the model, the ocean layers have thicknesses ranging from ~50 to 100 m. The LR version uses an eddy diffusivity of momentum about 100 times larger than that in the high-resolution (hereafter referred to as HR) version. The variations at all grid points throughout the world oceans are computed in the LR version. A 140-year simulation using the LR version has been completed. This experiment was conducted by the Climate Dynamics Project at GFDL and has been used as a control run for a study of the climatic effects of increasing carbon dioxide in the atmosphere. The ocean model in the HR version is the same as that analyzed by Philander and Siegel (1985) and has been demonstrated to mimic the actual oceanic changes when it was subjected to prescribed wind stress forcing for the 1982–83 warming event. Within the deep tropics, the meridional and zonal grid spacings in the HR model are 33 km and 100 km, respectively. In the upper 100 m of the ocean, the HR version has a vertical resolution of 10 m. In contrast to the LR version, ocean dynamics is incorporated only within the Pacific basin in the HR version, so that idealized boundaries need to be inserted in the western equatorial Pacific as well as along the northern and southern edges of the model domain. The sea surface conditions at maritime grid points outside of the Pacific are prescribed using observed climatological data. The HR version has been integrated for a total duration of 28 years. The basic experiments with the HR and LR versions have been conducted under annual mean insolation, so as to test the ability of the GCMs to reproduce realistic ENSO episodes in the absence of the annual time scale and other seasonally dependent climatological features.

It is apparent from the outset that the LR and HR integrations are suited for addressing different, but complementary, aspects of the ENSO problem. In view of its coarse resolution, the LR version cannot be expected to provide an adequate description of those wave modes in the equatorial ocean with spatial scales comparable to or less than the distance between neighboring grid points. For instance, equatorial Kelvin waves with typical meridional scales of 300 km would not be adequately represented in the LR model. Nonetheless, the worldwide extent of the active ocean domain in the LR model allows for the incorporation of realistic continental boundaries. The less demanding computer requirements of this version make it feasible to perform more extended integrations, so that the simulated ENSO-like events are much better sampled. On the other hand, the HR run should yield more detailed information on the propagation characteristics of different types of oceanic waves. However, the idealized vertical boundary situated at the western edge of the tropical Pacific in the HR version might cause excessive reflection of oceanic waves traveling into that region. With the considerably shorter (28-year) sample avail-

able, it is more difficult to assess the representativeness of the individual ENSO cycles appearing in the HR run.

A final noteworthy distinction between the LR and HR experiments is concerned with the nature of the initial conditions. The LR version has been integrated in an asynchronous coupling mode for 1250 ocean years prior to the present experiment (see Manabe and Stouffer 1988). Hence, the initial condition for the LR run is close to an equilibrium state of the coupled system. No such equilibrium has been sought with the HR version, so that the particular initial condition used for that experiment exerts a strong influence on subsequent model behavior.

We shall document the nature of ENSO-like phenomena simulated by the LR and HR versions in two articles. The present paper summarizes the results from the LR integration. The companion paper by Philander et al. (1992), which follows the present article in the same issue of this journal, is devoted to a description of the ENSO-like phenomena appearing in the HR experiment. The latter paper also contains a more detailed discussion of the similarities and differences between ENSO-like phenomena identified in the LR and HR runs, and in other simplified coupled models.

The structure of the LR coupled model is described in section 2. The climatological distributions of selected atmospheric and oceanic model variables are displayed in section 3. An overview of the gross ENSO-like features generated in the LR experiment is given in section 4. Common spatial and temporal characteristics shared by a majority of the ENSO-like events occurring in the integration are delineated by the extended empirical orthogonal function and regression analyses presented in section 5. In section 6 are shown the results from a diagnosis of both the time-mean and perturbation heat budgets for the top ocean layer near the equator, and the principal dynamical and physical processes operating in various stages of the model ENSO are noted. The last section summarizes the principal findings based on the LR run.

2. Description of the LR model

The atmospheric component of the coupled system used in this study is the spectral model developed and maintained by the Climate Dynamics Project at GFDL, and is essentially the same as that described by Manabe and Hahn (1981). The meteorological variables are represented by spherical harmonics with a rhomboidal truncation at wavenumber 15. The corresponding Gaussian grid has a horizontal resolution of approximately 7.5° longitude by 4.5° latitude. Vertical variations are represented at nine discrete atmospheric layers. Physical processes considered in the atmospheric model include radiative transfer, moist and dry convective adjustment, and subgrid-scale eddy diffusion. The bulk aerodynamic laws are used to parameterize the turbulent fluxes of moisture, sensible heat, and momentum within the planetary boundary layer. The atmospheric model also carries a full hydrologic cycle, which entails computations of precipitation, evaporation, and soil moisture content. However, the amount of cloud cover is prescribed as a function of latitude and pressure only. Realistic large-scale orography and land–sea contrast are incorporated at the lower boundary. The surface temperature over land is calculated diagnostically by assuming an exact local balance between radiative effects and latent and sensible heat fluxes. The surface temperature at maritime sites is determined by the oceanic component of the model.

The ocean model used for coupling with the atmosphere is similar to that described by Bryan and Lewis (1979) and has been developed by the Oceanic Circulation Project at GFDL. The three-dimensional distributions of oceanic variables are depicted by a finite-difference grid mesh with a horizontal spacing of 3.75° longitude by 4.5° latitude, so that two grid boxes of the ocean model fit exactly under each box in the atmospheric Gaussian grid. There are 12 oceanic model levels in the vertical direction. The thicknesses of the top four layers are 51, 68, 101, and 151 m. The eddy diffusion coefficient for horizontal momentum mixing used in the LR model is 2.5×10^5 m^2 s^{-1}. The corresponding value for vertical momentum mixing is 2×10^{-3} m^2 s^{-1}. The eddy diffusion coefficient for horizontal temperature and salt mixing varies from 5×10^3 m^2 s^{-1} at the surface to 1×10^3 m^2 s^{-1} in the deep ocean [see Eq. (8) of Bryan and Lewis (1979)]. For stable density stratification, vertical mixing of temperature and salt is accomplished by eddy diffusion with a coefficient increasing from 0.3×10^{-4} m^2 s^{-1} near the surface to 1.3×10^{-4} m^2 s^{-1} below the thermocline [see Eq. (9) of Bryan and Lewis (1979)]. In unstable cases, temperature and salinity are completely mixed throughout the unstable water column. Large-scale topography of the ocean floor is incorporated at the lower boundary.

The atmospheric and oceanic components of the model have been coupled at the air–sea interface through the interchange of water vapor, heat, and momentum. The moisture exchange occurs through precipitation, evaporation, and river runoff. Heat transfer across the ocean surface takes place in the form of radiative fluxes as well as sensible and latent heat fluxes. The atmospheric component imparts momentum to the oceanic circulation through the wind stress forcing. The coupling algorithm designed and coded by S. Manabe and R. Stouffer of the Climate Dynamics Project at GFDL has been used in the present experiment. In the course of the model run, the atmospheric model was first integrated forward by a model day with half-hour time steps. The oceanic conditions at the air–sea boundary were held fixed for the entire day. The

oceanic component was then integrated through the same model day with 3-hour time steps, with the upper boundary conditions being supplied by the (constant) daily averaged atmospheric forcing for that day. The initial conditions for the present experiment have been taken from the history tapes of a previous model run that has attained climatic equilibrium [see Experiment I described in Manabe and Stouffer (1988)]. The model was subjected to annually averaged insolation throughout the experiment. The model has been integrated for a total duration of approximately 140 years. The data for an 88-year segment in the latter part of this run have been extracted for the present analysis. Inspection of the temporal variations of selected parameters reveals no prominent secular trends in the model data, thus suggesting that the coupled system resides in a stable climatic regime during the period under investigation.

To ensure that the coupled model system yields a realistic distribution of sea surface salinity, the water flux adjustment procedure outlined in Manabe and Stouffer (1988) has been applied to the present integration. This adjustment method entails a preparatory integration of the coupled GCM (referred as the *RS* run in Manabe and Stouffer), during which the surface salinity was continuously restored to the local observed climatological values, with a time constant of 30 days. The time-averaged total surface water flux (hereafter referred to as F_{RS}) required to mimic the observed salinity distribution was computed. A measure of the systematic model bias was then estimated by evaluating the difference between F_{RS} and the sources and sinks of surface water as determined by internal model processes (i.e., precipitation plus river runoff minus evaporation, or $P + R - E$ in the notation used by Manabe and Stouffer). The correction factor $F_{COR} = F_{RS} - (P + R - E)$ was subsequently applied to the surface water flux at every time step in the 140-year integration described here.

The original intent of the above correction procedure is to produce a proper simulation of the thermohaline circulation in the North Atlantic. The amplitudes of the corrective flux F_{COR} are as high as 5 m yr^{-1} in the Greenland Sea region [see Fig. A1 of Manabe and Stouffer (1988)]. The flux adjustment applied in the tropical Pacific basin (not shown) are comparatively much weaker and seldom exceed 1 m yr^{-1}. These flux corrections result in a decrease in the salinity of the near-equatorial Pacific waters by ~1–1.5 ppt (compare Figs. 5a and 8a in Manabe and Stouffer). However, the climatological distributions of the SST field throughout the tropical Pacific in simulations with and without the adjustment are almost identical to each other (compare Figs. 4a and 7a in Manabe and Stouffer). In the tropical oceans, temperature variations generally play a more significant role in determining the water density than salinity variations. We could hence infer from the weak sensitivity of the tropical Pacific SST pattern to the water flux adjustment that this procedure has a minor impact on the model climatology in that region.

3. Model climatology

First we shall examine some of the long-term (88 years) averaged features simulated by the LR coupled model. In Fig. 1 are shown the mean distributions of (a) sea level pressure and (b) surface wind stress (arrows) and precipitation (stippling). In order to avoid the excessive extrapolations required for obtaining the sea level pressure field over the high terrains of Antarctica, values for the region south of 60°S are not shown in this figure. Under annual mean conditions, the simulated sea level pressure field (Fig. 1a) is characterized by a low pressure belt extending across almost the entire equatorial zone. Closed high pressure centers are simulated over the eastern subtropical oceans in both hemispheres. These features generally correspond well with those appearing in the observed pattern (e.g., see Hsu and Wallace 1976, Figs. 7–9). The meridional pressure gradients over the eastern portion of the tropical Pacific are seen to be weaker than the observed values. The wind stress pattern over the tropical oceans (Fig. 1b) is dominated by the northeasterly and southeasterly trades, with well-defined convergence zones located just north of the equator. The model wind stress field may be compared with the corresponding monthly observational charts documented by Hellerman and Rosenstein (1983, Fig. 4). The wind stress values over the eastern and central equatorial Pacific are approximately 50%–70% of the observed amplitudes. The tropical Pacific basin is characterized by copious rainfall in the west (see stippling in Fig. 1b) and almost arid conditions in the vicinity of the American coasts. The intense rainfall within the narrow intertropical convergence zones observed over much of the equatorial oceans (see Jaeger 1976; Dorman and Bourke 1979, 1981) is not apparent in the model simulation.

Although the model examined here has a global domain, we shall henceforth focus our attention on the simulation in the tropical Pacific. The time-averaged behavior of the model ocean in the Pacific basin is described in Fig. 2, which shows the patterns of (a) SST, (b) horizontal velocity (arrows) and upward motion (stippling) of the current in the top ocean layer, and (c) the vertical integral of ocean temperature over the top four ocean layers with a total depth of 371 m. The latter integral provides for a measure of the heat energy stored in the upper ocean and will hereafter be referred to as the "heat storage." The most notable features in the SST field (Fig. 2a) are the cold tongue of surface water extending from the Peru–Ecuador coast toward the central equatorial Pacific, and the warm bodies of water straddling this cold region on

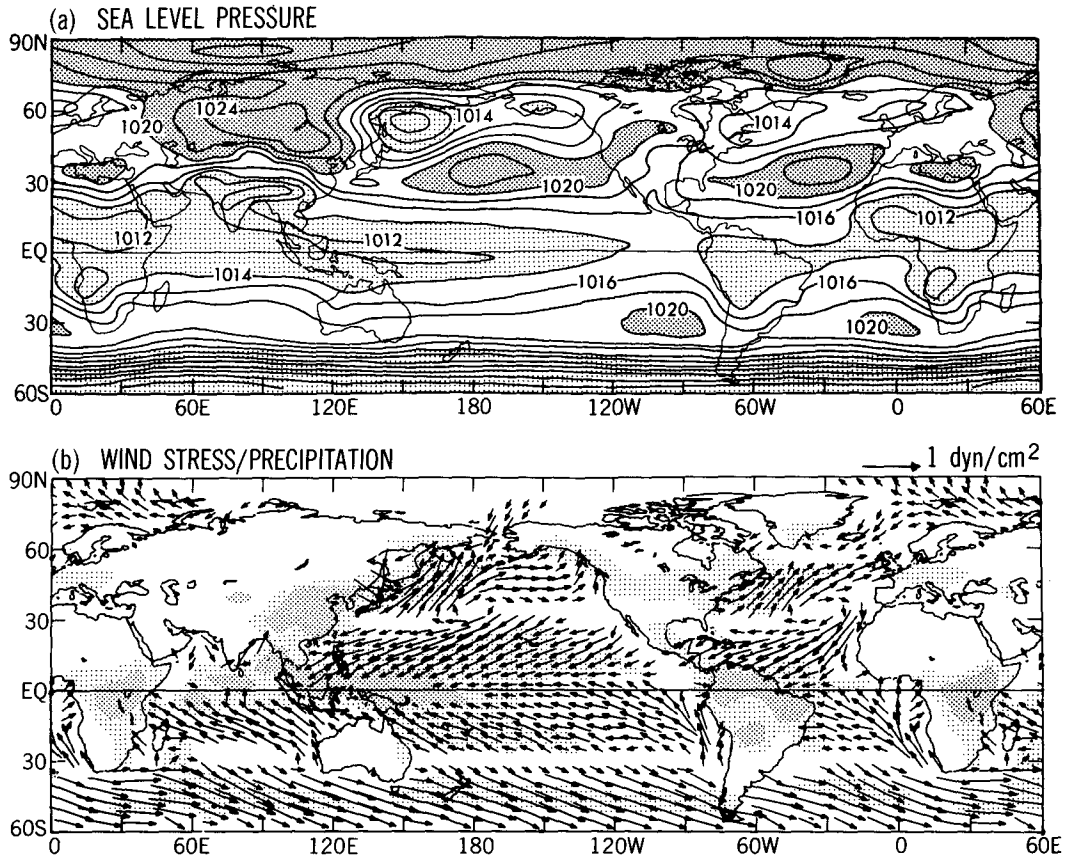

FIG. 1. Model climatology of (a) sea level pressure (contour interval: 2 mb) and (b) surface wind stress (arrows) and precipitation rate (stippling). The scale for the wind stress vectors is given in the upper right corner of panel (b). Arrows too short to show up clearly have been omitted. Light stippling in panel (b) indicates rainfall rates between 3 and 5 mm day^{-1}, dense stippling indicates values exceeding 5 mm day^{-1}.

both sides of the equator. The warmest waters reside in the tropical western Pacific. The overall pattern in Fig. 2a is in agreement with the observations (e.g., see Horel 1982, Fig. 1). However, the model ocean produces a relatively less intense cold tongue, so that the simulated horizontal SST gradients are weaker than the observed values. The predominantly westward surface flow is accompanied by meridional divergence and upwelling in the tropical region (Fig. 2b). Upon arriving at the western boundary, the equatorial currents are deflected poleward along the East Asian and Australian seaboards. However, some of the Pacific waters flow through the open passage between New Guinea and Borneo (in particular, note the southward velocity vector in that location) and eventually make their way to the Indian Ocean. There is no evidence in the model pattern of the observed North Equatorial Countercurrent within the 3°–10°N zone. The unrealistically weak cold tongue and upwelling near the eastern edge of the Pacific are likely related to the inadequate resolution of the coastal ocean dynamics by the LR model, as well as the weak wind stress forcing (see Fig. 1b). The pattern for the ocean heat storage (Fig. 2c) bears some resemblance to that of the SST field (Fig. 2a). However, the equatorial cold tongue is much less apparent in the heat storage distribution. The largest heat storage is found in the western Pacific south of the equator. The tropical waters farther east and farther north are characterized by considerably smaller heat storage.

The subsurface thermal structure and current systems of the ocean model are illustrated by the longitude–depth and latitude–depth cross sections of selected variables in Figs. 3 and 4, respectively. In accord with the observations (e.g., see Colin et al. 1971), the simulated temperature contours in the equatorial Pacific generally slope upward from west to east (Fig. 3a). The crude vertical resolution of the model precludes an accurate depiction of the mixed layer near the surface, as well as the enhanced vertical temperature gradients in the thermocline region. The cross section for the zonal current speed (Fig. 3b) indicates that, throughout the equatorial Pacific, a weak eastward current exists just under the westward current at the surface.

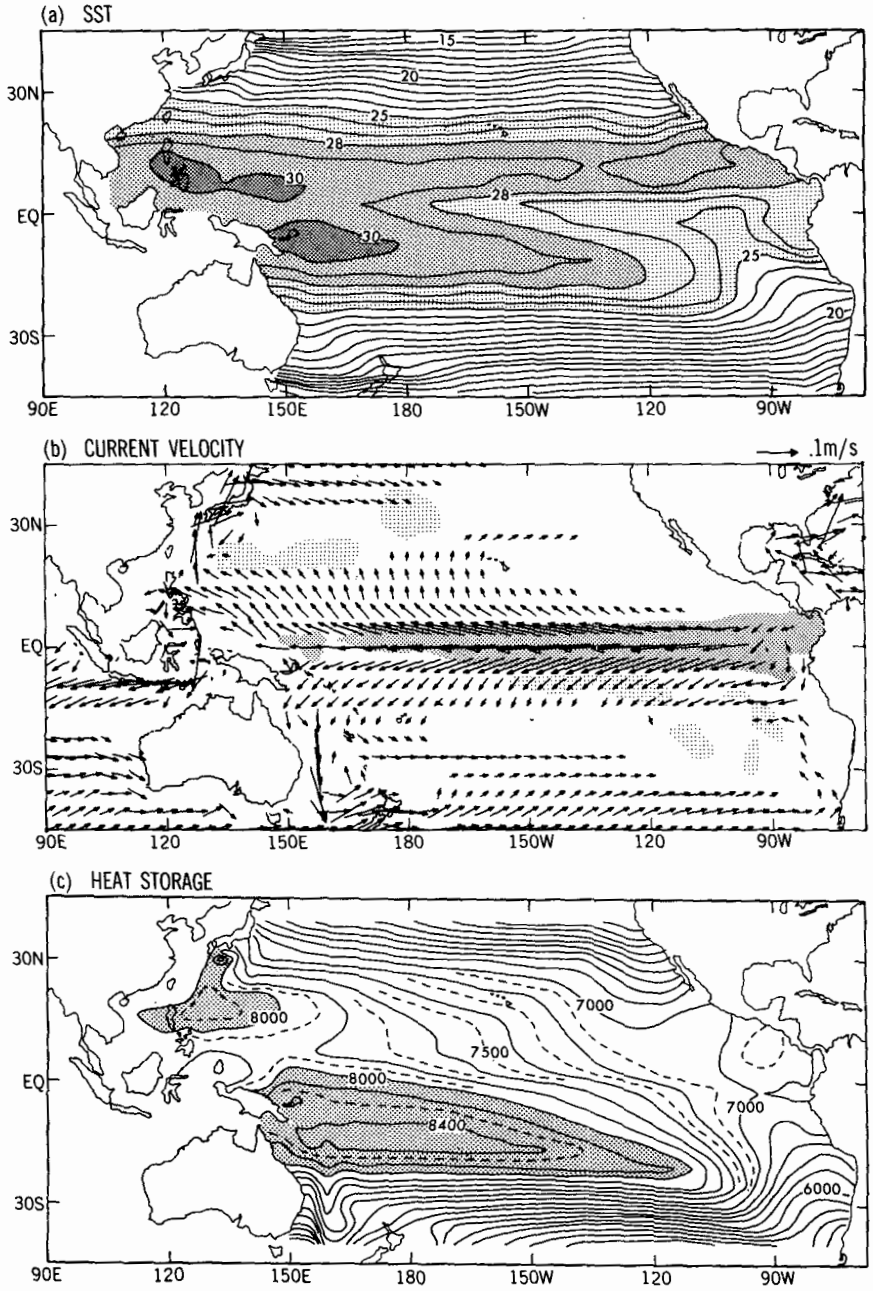

FIG. 2. Model climatology of (a) sea surface temperature (contour interval: 1°C), (b) horizontal velocity of the surface current (arrows) and vertical velocity at the base of the top ocean layer (stippling), and (c) ocean heat storage (contour interval: 200°C m), as obtained by integrating the temperature with depth through the top 371 m of the ocean model. The scale for the horizontal velocity vectors is given in the upper right corner of panel (b). Arrows too short to show up clearly have been omitted. Light and dense stippling in panel (b) indicate downwelling and upwelling motions exceeding 1×10^{-6} m s^{-1}, respectively.

The most notable feature in the meridional cross section of the temperature field within the 120°–150°W zone (Fig. 4a) is the shoaling isotherms near the equator. Comparison of the zonal currents appearing in Fig. 4b with the corresponding observations (e.g., see Knauss 1978, Fig. 8.15; Bryden and Brady 1985, Fig. 8) reveals the absence of the North Equatorial Countercurrent and a simulated equatorial undercurrent that is weaker than its observed counterpart by an order of magnitude. It is also evident that the characteristic

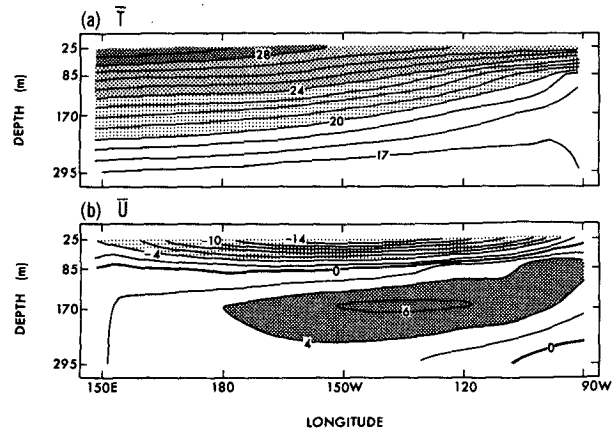

FIG. 3. Longitude–depth distributions of the model climatology of (a) temperature ($\bar{T}$, averaged between 6.75°S and 6.75°N; contour interval: 1°C) and (b) zonal current speed ($\bar{u}$, averaged between 4.5°S and 4.5°N; contour interval: 2×10^{-2} m s^{-1}) of the upper ocean.

meridional scale of the current systems in the ocean model is considerably larger than the actual measurements. The cross section in Fig. 4c indicates that meridional outflow from the equator prevails in the surface layer, whereas meridional inflow occurs at about 90-m depth. This circulation pattern is linked to upwelling at the equator and downwelling in higher latitudes (Fig. 4d). The oceanic circulation along the meridional plane is in qualitative agreement with that inferred from the mass budget analysis of the HR model (Philander and Hurlin 1988). The magnitudes of the near-surface zonal current and upwelling in the simulation are weaker than observational estimates (e.g., Bryden and Brady 1985) by as much as a factor of 10. Since most of the model deficiencies noted in various panels of Fig. 4 are not evident in the HR version (see Philander et al. 1992, Fig. 4), they are attributable to the coarse resolution and the large eddy diffusivity used in the present experiment.

4. General characteristics of simulated ENSO-like features

In this section we shall give a brief overview of the typical time scale and propagation behavior of ENSO-like events appearing in the model experiment, as well as the interrelationships among various atmospheric and oceanic fluctuations associated with ENSO. Minimal processing has been applied to the data displayed here, so as to demonstrate that the gross features of ENSO are discernible from the raw model output. These basic results hence complement the findings based on more elaborate analyses in the following sections.

The temporal variation of the SST anomaly averaged over the central equatorial Pacific during an 80-yr period of the experiment is shown in Fig. 5. Both the monthly averaged values (thin curve) and the 7-month running means (thick curve) are displayed in this diagram. This time series is indicative of the presence of recurrent oscillations in the SST field. The time interval between anomalies of the same polarity is typically 3–4 years. In certain periods of the experiment, the individual warm and cold events appear to be modulated by a low-frequency signal with a time scale of 6–8 years. For instance, the above-average SSTs in years 1–4 and years 67–71 are followed by prolonged cold periods in years 7–11 and years 75–78, respectively. The amplitudes of the warm and cold events range between 0.5° and 1°C and are weaker than the observed values in the same region (see Rasmusson and Carpenter 1982, Fig. 11).

The dominant time scales of the SST fluctuations in the central equatorial Pacific are further illustrated by the spectrum in Fig. 6. This spectrum was obtained by applying the lag-correlation method to monthly mean data. No additional smoothing has been applied to the SST time series beyond the monthly averaging procedure. Two spectral peaks at time scales of 66–80 and 33–40 months are evident in this figure. The en-

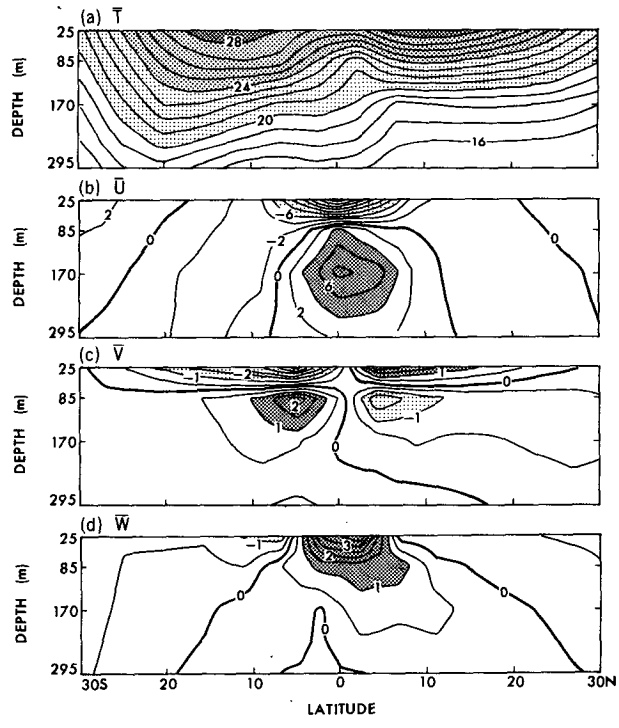

FIG. 4. Latitude–depth distributions of the model climatology of (a) temperature ($\bar{T}$, contour interval: 1°C), (b) zonal current speed ($\bar{u}$, contour interval: 2×10^{-2} m s^{-1}), (c) meridional current speed ($\bar{v}$, contour interval: 5×10^{-3} m s^{-1}), and (d) vertical current speed ($\bar{w}$, contour interval: 5×10^{-7} m s^{-1}) of the upper ocean. Panels (a) and (d) show averages of the model data between 122° and 152°W. Panels (b) and (c) show averages over the 120°–150°W zone.

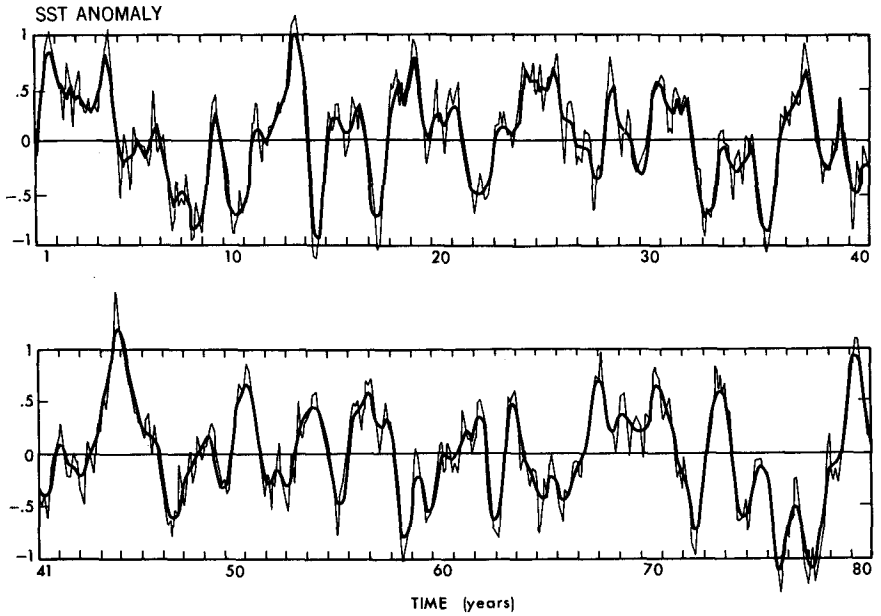

FIG. 5. Time series of the sea surface temperature anomaly averaged between 2.25°S and 2.25°N, 165°E and 165°W during an 80-year segment of the model experiment. The thin curve represents fluctuations of the monthly mean values. The thick curve depicts variations of 7-month running means.

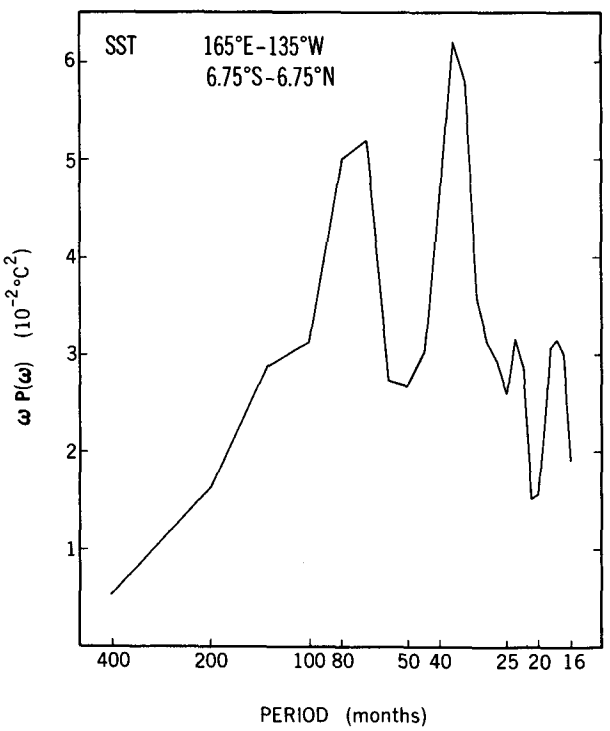

FIG. 6. An area-conserving version of the power spectrum of the sea surface temperature averaged between 6.75°S and 6.75°N and between 165°E and 135°W. The ordinate is the product of frequency and spectral density. The abscissa is the logarithm of frequency.

hanced power within these two period ranges is consistent with our visual impression of the time series in Fig. 5. Since the spectral peak at the 33–40-month period appears to be more relevant to the growth and decay of individual warm and cold episodes in Fig. 5, and spectra of observed SST data for the 1953–74 period also exhibit maxima at the 3–4-year time scale (e.g., see Rasmusson and Carpenter 1982, Fig. 6), we shall henceforth devote our attention exclusively to this time scale. The nature of the phenomena associated with the 66–80-month peak is worth further study. However, an adequate sampling of these low-frequency features would require a model run that is even longer than the one attempted here.

In Fig. 7 is shown the time–longitude distribution of the near-equatorial SST field for years 41–60, during which the warm and cold events are particularly active. A 3-month running mean has been applied to the monthly data. It is seen that the SST fluctuations attain the highest amplitudes in the central portion of the ocean basin. The variability immediately off the South American coast is relatively lower. This plot also reveals that most of the temperature extrema make their first appearance in the eastern Pacific and then migrate progressively westward with time. A case in point is the warm event in years 44–45, during which the SST has peaked at 100°W by the beginning of year 44, whereas maximum warming at the date line does not occur until the end of the same year. The warm events

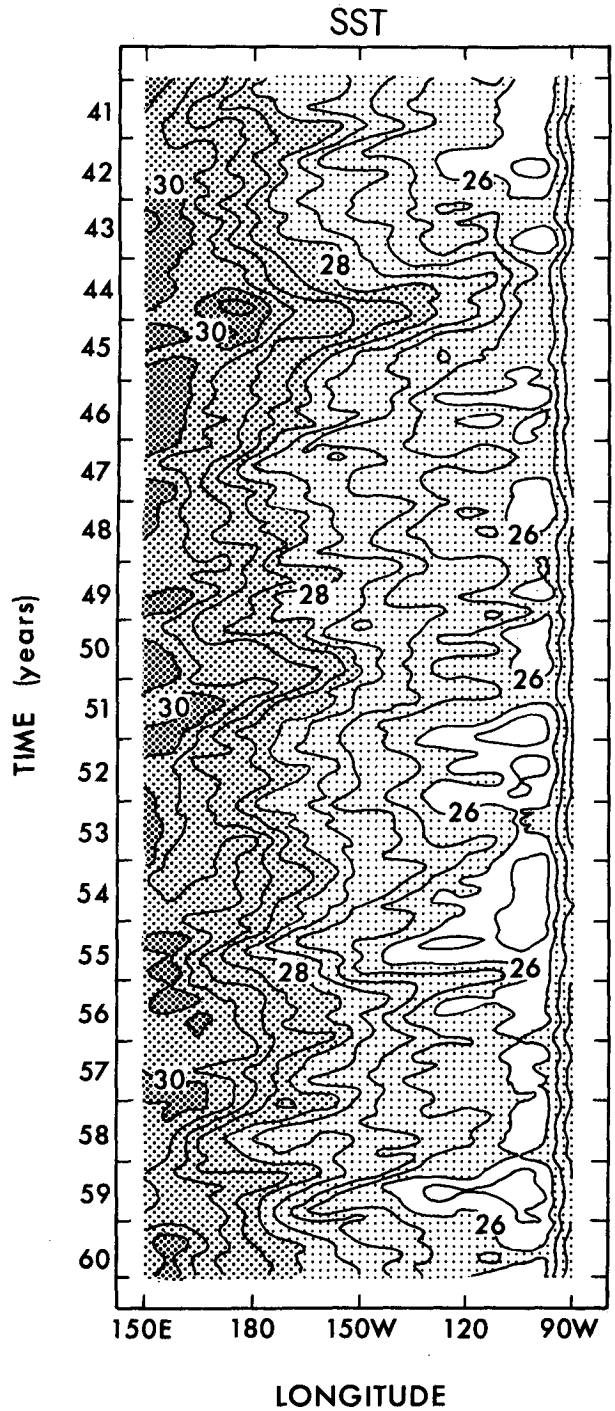

FIG. 7. Longitude–time distribution of the sea surface temperature averaged between 2.25°S and 2.25°N for a 20-year segment of the model experiment. Contour interval: 0.5°C. The values have been smoothed by a 3-month running mean filter.

in years 50–51, 53–54, and 56–57 and the cold events in years 46–47, 54–55, and 59–60 exhibit a similar behavior.

The concomitant atmospheric and oceanic changes accompanying the warm and cold events are illustrated in Fig. 8, which shows the variations of selected circulation indices for the central equatorial Pacific during years 41–60. The model data displayed in this figure include anomalies in (a) SST, (b) zonal wind at 990 mb, (c) Southern Oscillation index, defined as the sea level pressure difference between Tahiti and Darwin, (d) precipitation rate, and (e) zonal current speed within the top ocean layer. It is evident from these time series that SST anomalies are positively correlated with eastward near-surface zonal wind, precipitation, and eastward surface current and negatively correlated with the Southern Oscillation index. This set of relationships are in accord with the well-known circulation changes observed in ENSO episodes (e.g., see Rasmusson and Wallace 1983). When compared with the corresponding fluctuations appearing in the HR model (see Philander et al. 1992, Fig. 5), the amplitudes of the anomalies shown in Fig. 8 are noticeably lower.

The contrast between the instantaneous circulation patterns prevailing in the warm and cold phases of the simulated events is illustrated in Figs. 9 and 10. In these diagrams are mapped the distributions of SST, horizontal surface ocean current, upwelling, ocean heat storage anomaly, sea level pressure, surface wind stress, and precipitation rate for months 10–12 of year 44, which coincide with the peak of the most outstanding warm episode in the model record (see Figs. 5, 7, and 8), and for months 7–9 of year 47, which correspond to the succeeding period of maximum cooling.

During the warm period, equatorial waters with temperature surpassing 30°C extend eastward beyond the date line, and the cold tongue is confined to the eastern Pacific (Fig. 9a). The cold tongue is much more prominent in the cold phase, and nowhere along the equator does the SST exceed 30°C (Fig. 9b). The near-equatorial horizontal currents and upwelling at the ocean surface are noticeably weaker in the warm episode (Fig. 9c) than in the cold episode (Fig. 9d). In Fig. 9e, the pattern of ocean heat storage (see definition in section 3) for the warm event indicates the presence of a positive anomaly along the equator in the central and eastern Pacific, and negative anomalies in the regions farther north and farther south. Below-normal heat storage is simulated along the equator during the cold event (Fig. 9f).

Within the atmosphere, the warm period is characterized by a weakening and eastward displacement of the equatorial low pressure center toward the date line and relaxation of the sea level pressure gradients in the central tropical Pacific (Fig. 10a). The pressure gradients are relatively stronger in the eastern equatorial Pacific in the cold period (Fig. 10b). The wind stress charts (Figs. 10c and 10d) indicate weaker atmospheric surface flows near the equator in the warm event. Enhanced rainfall near the date line occurs at the peak of

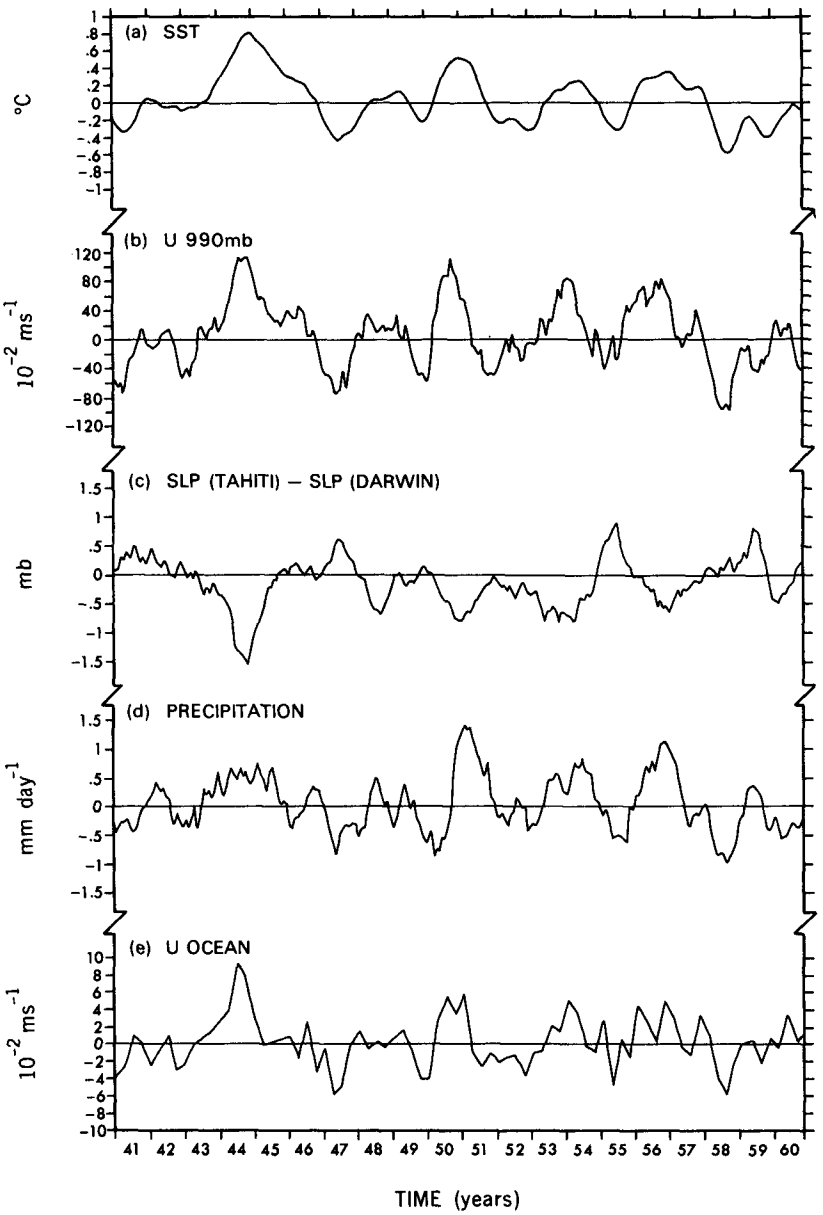

FIG. 8. Time series of the anomalies in (a) sea surface temperature, (b) zonal wind at 990 mb, (c) sea level pressure difference between Tahiti and Darwin, (d) precipitation rate, and (e) zonal current speed of the top ocean layer during a 20-year segment of the experiment. Panels (a), (b), and (d) show averages of the model data between 6.75°S and 6.75°N and between 165°E and 165°W. The curve in panel (e) represents the areal means over the region between 4.5°S and 4.5°N and between 165°E and 165°W. The values in panels (a)–(d) are based on 7-month running means. Seasonal mean values are plotted in panel (e).

the warming (see stippling in Fig. 10c); whereas the heaviest precipitation is restricted to the Indonesian sector during the cold period (Fig. 10d). Some of the circulation patterns presented in Figs. 9 and 10 may be compared with the corresponding observational charts, such as those compiled by Ramage et al. (1980) and Arkin et al. (1983) for the 1972–73 and 1982–83 events, respectively. It is seen that some of the observed ENSO phenomena in the central Pacific are captured by the simulation. However, the large variability observed near the South American coast (east of 90°W) during ENSO is not evident in the model results.

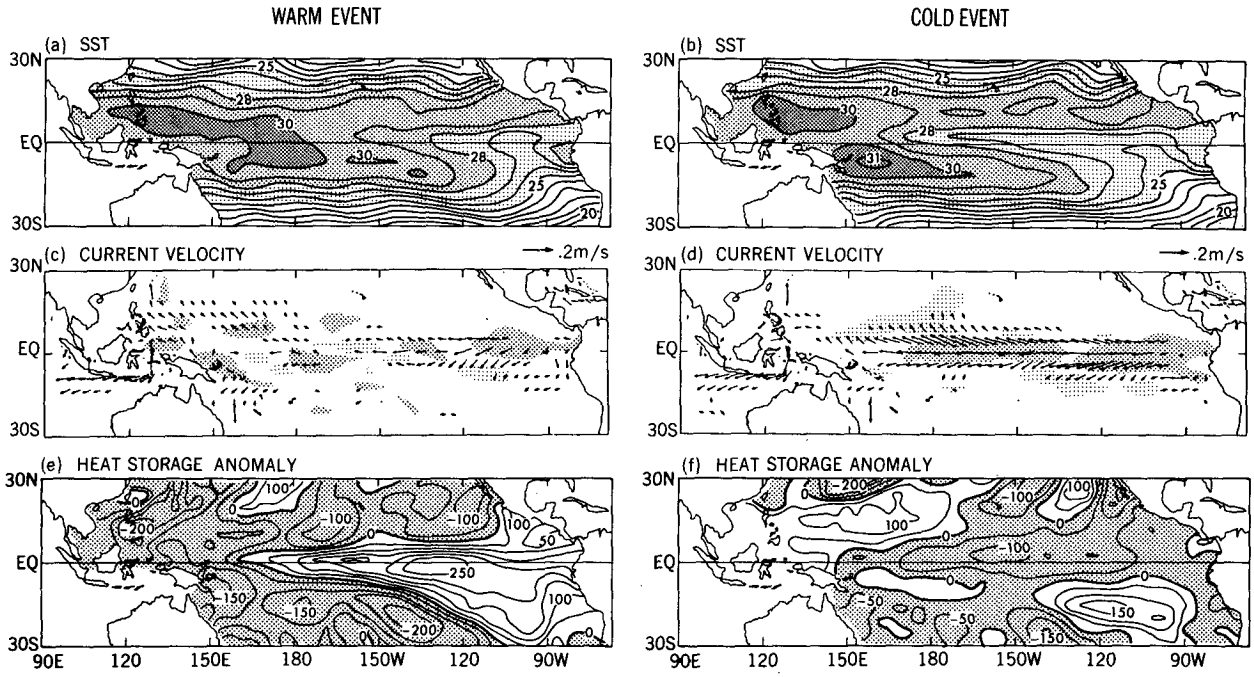

FIG. 9. Distributions of sea surface temperature (contour interval: 1°C) during (a) the warm episode occurring in year 44, month 10–12, and (b) the cold episode occurring in year 47, month 7–9; of horizontal current velocity (arrows) and vertical current speed (stippling) at the top ocean layer during the (c) warm and (d) cold episodes; and of ocean heat storage anomaly (contour interval: 50°C m) during the (e) warm and (f) cold episodes. The scale for the current velocity vectors is given at the upper right corner of panels (c) and (d). Arrows too short to show up clearly have been omitted. Dense and light stippling in panels (c) and (d) indicate upwelling and downwelling exceeding 2×10^{-6} m s^{-1}, respectively.

5. Typical space–time evolution of simulated ENSO events

a. The extended EOF analysis procedure

The evidence presented in the previous section indicates that some of the observed ENSO features are mimiced in two outstanding episodes in the experiment. In view of the multitude of warm and cold events appearing in the entire 88-year dataset available for the present study (see Fig. 5), it is of interest to determine whether most of these events exhibit the ENSO-like behavior noted in the special cases examined thus far. We shall address this issue by applying an extended empirical orthogonal function (EEOF) analysis to

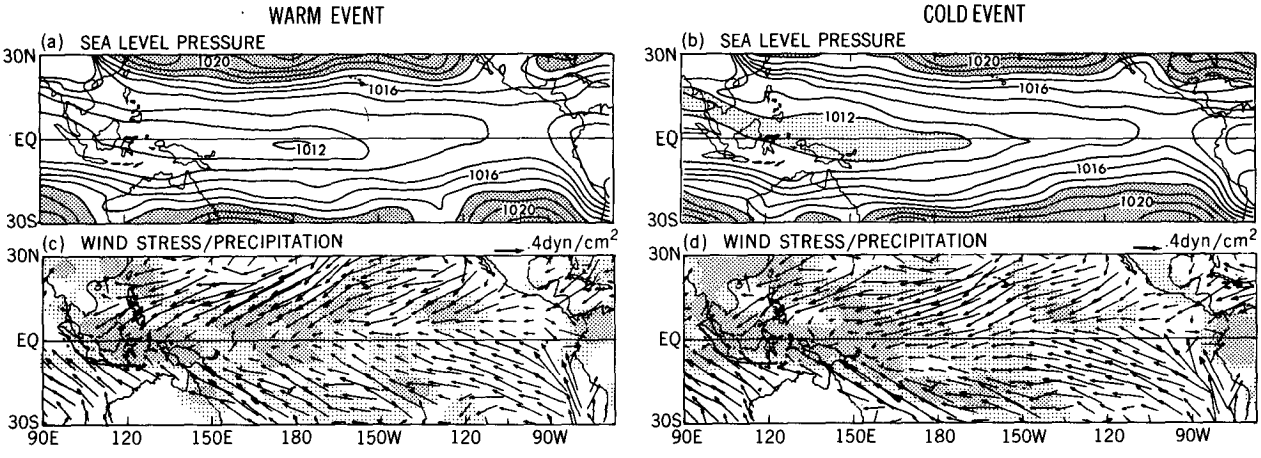

FIG. 10. As in Fig. 9, but for sea level pressure [panels (a) and (b); contour interval: 1 mb] and for surface wind stress (arrows) and precipitation rate (stippling) [panels (c) and (d)]. The scale for the wind stress vectors is given at the upper right corner of panels (c) and (d). Light and dense stippling in these panels indicate precipitation rates within the ranges of 3–5 and >5 mm day^{-1}, respectively.

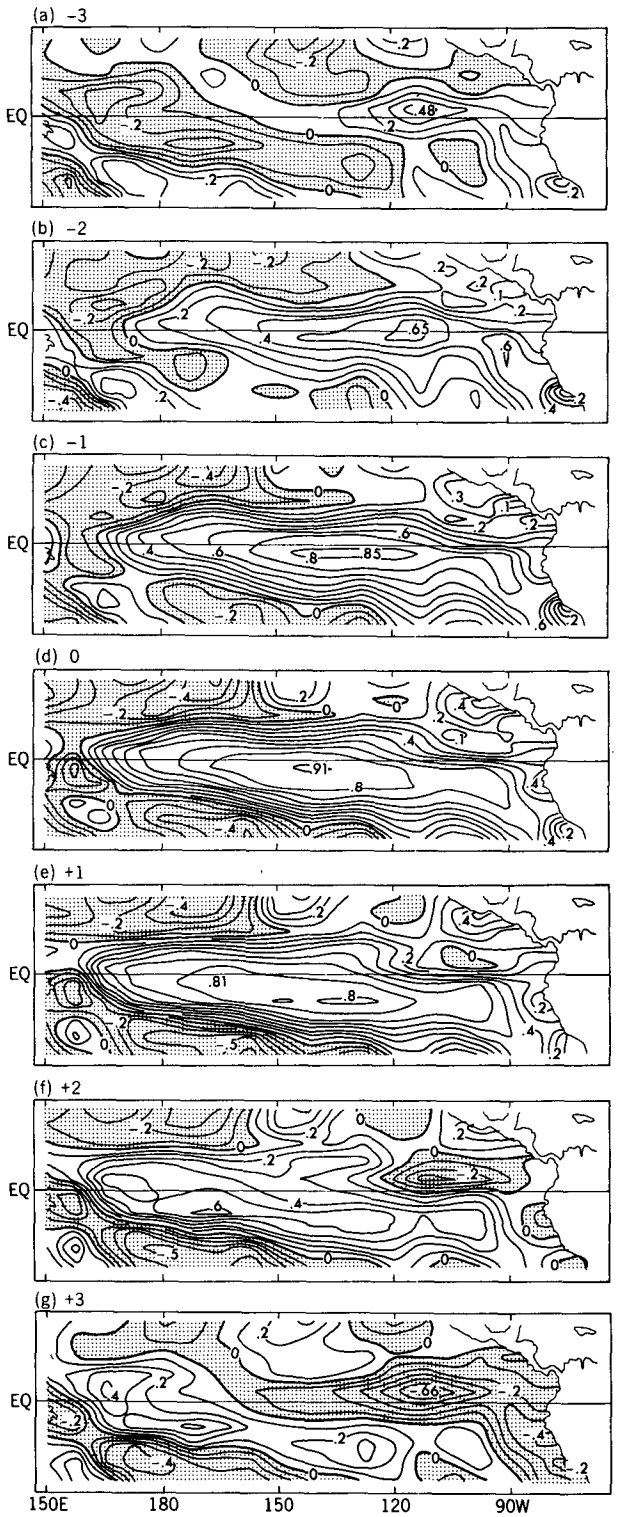

FIG. 11. Distributions of the correlation coefficients between the temporal coefficients of the leading EEOF [$c_1(t)$] for the SST field and the SST data at individual grid points, as obtained with $c_1(t)$ *lagging* the gridpoint data by (a) 3, (b) 2, (c) 1, and (d) 0 seasons; and with $c_1(t)$ *leading* the gridpoint data by (e) 1, (f) 2, and (g) 3 seasons. Contour interval: 0.1. Although the experiment analyzed here has been conducted under annually averaged conditions, the term "season" is used to denote the unit time interval of 90 days in this and some of the following figures.

identify the most recurrent modes of evolution of selected data fields in the spatial and temporal domains. In essence, this tool is an extension of the conventional EOF analysis with the inclusion of lagged correlation values in the cross-correlation matrix. A detailed description of the EEOF technique has been given by Weare and Nasstrom (1982) and Lau and Chan (1985).

In the present study, the EEOF analysis has been conducted separately for SST, sea level pressure, zonal wind stress, zonal current speed of the top ocean layer, and ocean heat storage (see definition in section 3). In order to emphasize the zonally asymmetric component of the sea level pressure fluctuations, the zonal mean values for each time interval have been subtracted from the local gridpoint values for the same time interval before the pressure data were subjected to further processing. The domain of analysis extends from 20°S to 20°N and from 150°E eastward to the American coasts. The spatial variations of the data fields are represented by a grid mesh with zonal and meridional spacings of 15° and 4.5°, respectively. The grid points along neighboring latitude rows are staggered with respect to each other. The number of grid points for the SST, pressure, wind stress, and heat storage fields is 89, whereas the grid for the zonal current consists of 84 points. The EEOF analysis was performed on data averaged over 90-day intervals, with the number of time lags [$J + 1$ in the notation of Lau and Chan (1985)] being set to 7. For the sake of convenience, each unit time interval ($\tau = 90$ days, see notation used by Lau and Chan) will be referred to as a "season," always keeping in mind that the model integration has been conducted in the absence of a seasonal cycle. The maximum time lag possible, as given by $(7 - 1)\tau = 6$ seasons, corresponds to approximately one-half of the averaged period of the ENSO cycles appearing in the experiment. In order to focus on circulation features relevant to ENSO, the model data have been subjected to a 61-point digital filter prior to the EEOF analysis so as to retain fluctuations with periods ranging from 8 to 17 seasons. The model data at a given grid point have been normalized by the temporal standard deviation at the same grid point, so that the elements of the matrix in the eigenvalue problem are actually correlation coefficients.

b. *Eigenvectors of the SST field*

The first eigenvector e_1 obtained by applying the EEOF analysis to the SST field explains 13.3% of the domain-integrated variance. In Fig. 11 are shown the

set of seven spatial patterns corresponding to e_1. These charts, often referred to as the "loading patterns" of e_1, were computed using the following procedure.

- The temporal coefficients $c_1(t)$ of e_1, which provide for a measure of the resemblance of the data at time t to the space–time evolution portrayed by e_1, were first evaluated by forming the dot product of e_1 and the seven-season sequence of SST fields centered at t.
- Temporal correlation coefficients between $c_1(t)$ and the SST values at individual grid points in the analysis domain were then computed separately for lags of 0, ±1, ±2, and ±3 seasons.
- The spatial patterns of the correlation coefficients thus obtained were mapped in Fig. 11. The panels in this figure have been arranged in the order of increasing time lag, so that the top panel (a) illustrates the results for $c_1(t)$ *lagging* the SST data by three seasons, and the bottom panel (g) shows the correlation values for $c_1(t)$ *leading* the SST data by three seasons.

The sequence of charts in Fig. 11 may be interpreted as a depiction of the temporal evolution of the dominant SST anomaly pattern during seven successive seasons. These patterns indicate that a SST anomaly of a given polarity makes its first appearance off the Peru–Ecuador coast and in the eastern equatorial Pacific near 105°W [see panel (a)] and subsequently migrates westward. Four seasons later [panel (e)], the center of the anomaly almost arrives at the date line, whereas the equatorial waters in the eastern Pacific and near the American coasts are gradually returning to normal temperatures. After two additional seasons [panel (g)], the SST anomaly reaches its westernmost extent, and a new anomaly with the opposite polarity emerges in the eastern half of the basin. Except for a sign reversal, the patterns in panels (a) and (g) are almost identical to each other, thus indicating that the mode of space–time variability under investigation evolves through a half-cycle in approximately six seasons. Considering the cyclical nature of the phenomenon at hand, the subsequent development of the emergent anomaly in panel (g) would follow the patterns depicted in panels (a)–(f) but with the polarity reversed. The behavior of the model-simulated SST field in the above scenario is in broad agreement with the development of composite anomalies associated with observed ENSO events during the 1950–73 period, as documented by Rasmusson and Carpenter (1982).

The set of patterns for the second eigenvector e_2 (not shown), which explains 11.4% of the total variance, is almost identical to the set for e_1, except that the time sequence for e_2 lags the sequence depicted in Fig. 11 by three seasons. The time series of the two leading eigenvectors (c_1 and c_2) also exhibit a strong quadrature relationship with each other. It is well known that a propagating signal of the type described in Fig. 11 is represented by a pair of eigenvectors of comparable variance and in spatial and temporal quadrature with each other. The total variance explainable by the westward-migrating SST mode described in Fig. 11 is hence equal to the sum of the variances attributed individually to e_1 and e_2, that is, 24.7%.

c. *Eigenvectors of other variables*

In analogy with the results for the SST field described in the preceding subsection, application of the EEOF analysis to each of the sea level pressure, zonal wind stress, zonal surface current, and ocean heat storage fields also yields two leading eigenvectors that bear a temporal quadrature relationship to each other. The leading pairs of eigenvectors for the pressure, wind stress, zonal current, and heat storage data account for 35.4%, 16.8%, 26.4%, and 38.4%, respectively, of the domain-integrated variance of the corresponding parameter.

The space–time behavior of the leading eigenvectors of different variables is depicted in Fig. 12. Each of the panels in this figure displays the lagged correlation coefficients between the coefficients for the first eigenvector [$c_1(t)$, see definition in section 5b] of a given variable x and the model data for x at individual grid points along the equatorial zone. The ordinate of these panels corresponds to the time lag between $c_1(t)$ and the grid-point data and ranges from −6 seasons to +6 seasons. Longitudinal variations along the equatorial Pacific for individual time lags are depicted along the abscissa. The variables displayed in this manner are (a) SST, (b) sea level pressure, (c) zonal wind stress, (d) zonal surface current speed, and (e) ocean heat storage.

The pattern in Figs. 12a–d confirm that the leading eigenvectors independently obtained for SST, sea level pressure, zonal wind stress and zonal surface current are all characterized by westward-traveling extrema along the equator. The typical time scale for a complete cycle in such events is also approximately 12 seasons. Westward propagation is not evident in the pattern for ocean heat storage (Fig. 12e). The latter result indicates that heat storage anomalies throughout the central and eastern Pacific attain their maximum strength at approximately the same time, whereas corresponding anomalies in the extreme western Pacific tend to lead the changes farther east by a quarter-cycle.

As a measure of the extent to which the first eigenvectors of different oceanic and atmospheric fields are linked to each other, simultaneous correlation coefficients have been computed between the temporal coefficients for the first eigenvector [$c_1(t)$] of a certain variable and the corresponding coefficients of another variable. The matrix of correlation coefficients thus obtained for all possible pairs of variables is displayed in Table 1. It is seen that the time series $c_1(t)$ for a

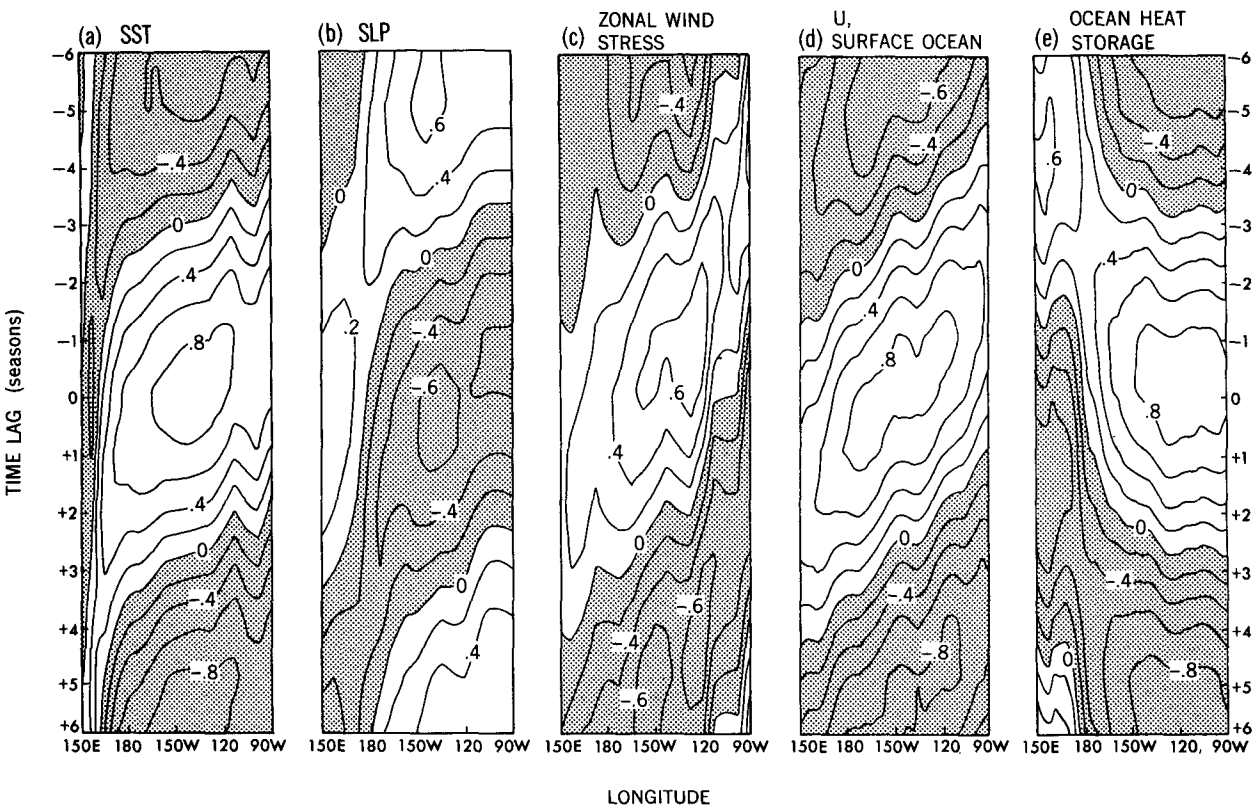

FIG. 12. Longitude–time lag distributions of the correlation coefficients between the temporal coefficients of the leading EEOF [$c_1(t)$] for (a) SST, (b) sea level pressure (SLP), (c) zonal wind stress, (d) zonal surface current, and (e) heat storage of the upper ocean and the corresponding data at individual grid points near the equator (contour interval: 0.2). For panels (a), (b), (c), and (e), the model data at the grid points between 6.75°S and 6.75°N have been averaged prior to the correlation analysis. The results in panel (d) were based on averages between 4.5°S and 4.5°N. Negative (positive) time lags indicate gridpoint data leading (lagging) $c_1(t)$.

given variable is highly correlated with the corresponding time series for all other variables considered here. Hence, there is little doubt that the ENSO cycle manifests itself as the leading mode of space–time evolution for all five model fields examined here.

TABLE 1. Matrix of correlation coefficients between the temporal coefficients of the leading EEOF [i.e., $c_1(t)$, see definition in text] for different model variables. All values are expressed in percent.

	SST	Zonal wind stress	Sea level pressure	Zonal surface current	Ocean heat storage
SST	100	77	80	64	94
Zonal wind stress		100	79	76	74
Sea level pressure			100	86	80
Zonal surface current				100	68
Ocean heat storage					100

d. Regression patterns associated with the leading EEOF mode

In this subsection, the typical sequence of events occurring in the course of the simulated ENSO-like events is described. The temporal coefficients of the first EEOF of the SST field [$c_1(t)$, see definition in section 5b] is chosen as the reference time series for defining the temporal evolution of the ENSO events. Following the analysis technique outlined by Nakamura et al. (1987), regression coefficients have been computed between gridpoint values of selected model variables and this reference time series at different time lags. The spatial distributions of the regression coefficients for individual lags, hereafter referred to as regression patterns, may be interpreted as the weighted composite fields of the simulated anomalies in different phases of the ENSO-like cycle. The regression patterns thus obtained are displayed in Fig. 13 for sea level pressure (contours) as well as zonal and meridional components of the surface wind stress (arrows), and in Fig. 14 for ocean heat storage (contours) and the horizontal velocity

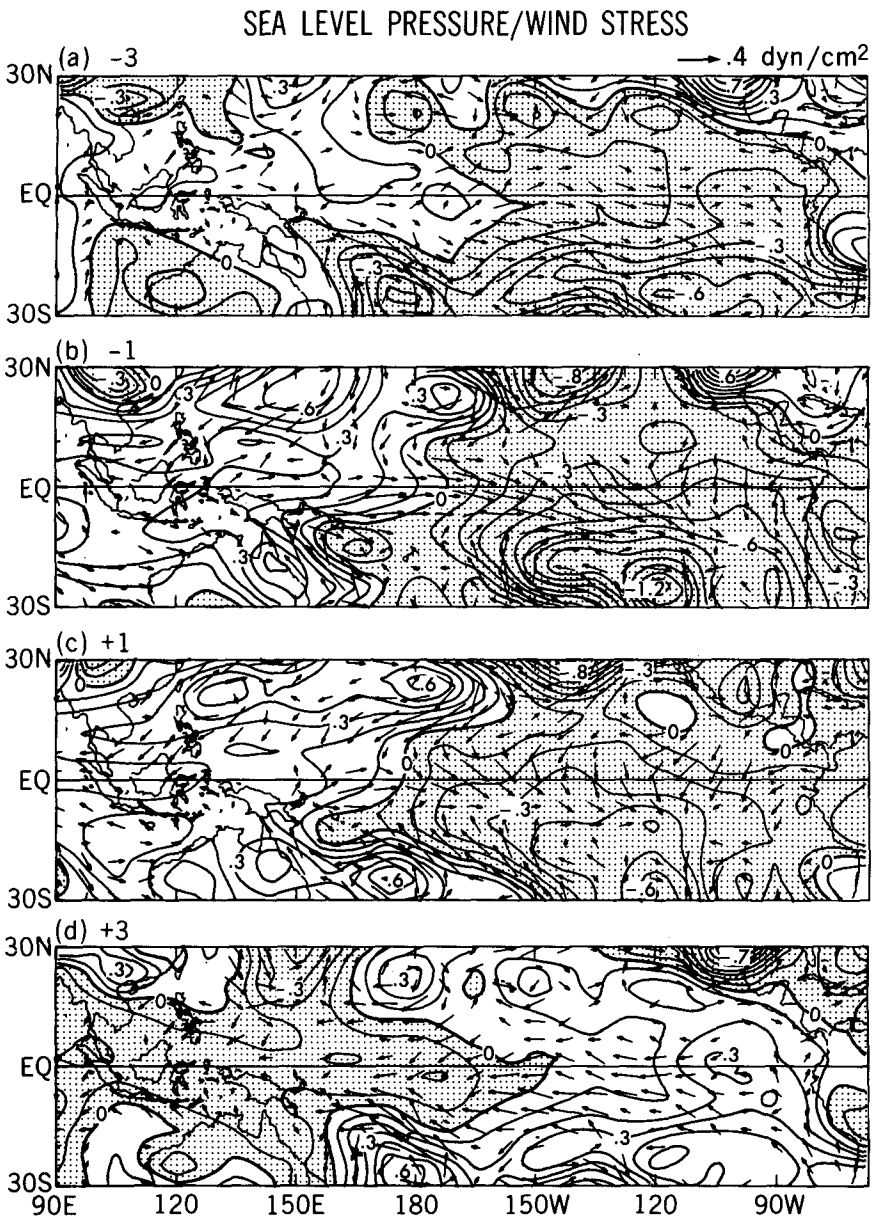

FIG. 13. Distributions of the linear regression coefficients between $c_1(t)$ of the SST field and the gridpoint values of sea level pressure (SLP, contours; interval: 0.1 mb) and surface wind stress vector [arrows; see scale at the upper right corner of panel (a)], as obtained with $c_1(t)$ *lagging* the gridpoint data by (a) 3 and (b) 1 seasons; and with $c_1(t)$ *leading* the gridpoint data by (c) 1 and (d) 3 seasons.

vector at the top ocean layer (arrows). The four panels in each of these figures display the regression values for time lags ranging from −3 to +3 seasons. By viewing these panels in succession from top to bottom, one may gain an impression of the representative chain of events occurring at 6-month intervals through the warm half of the ENSO-like cycle. The peak of the warm phase occurs near zero lag in this time frame (see Fig. 11d). The model behavior pertinent to the cold half of the cycle may be discerned in a similar manner by reversing the polarity of all the patterns in these figures. The time series $c_1(t)$ has been multiplied by a time-invariant factor so that the regression coefficients for the SST field (not shown) in the central equatorial Pacific attain maximum values of approximately 1 °C. The regression coefficients shown in Figs.

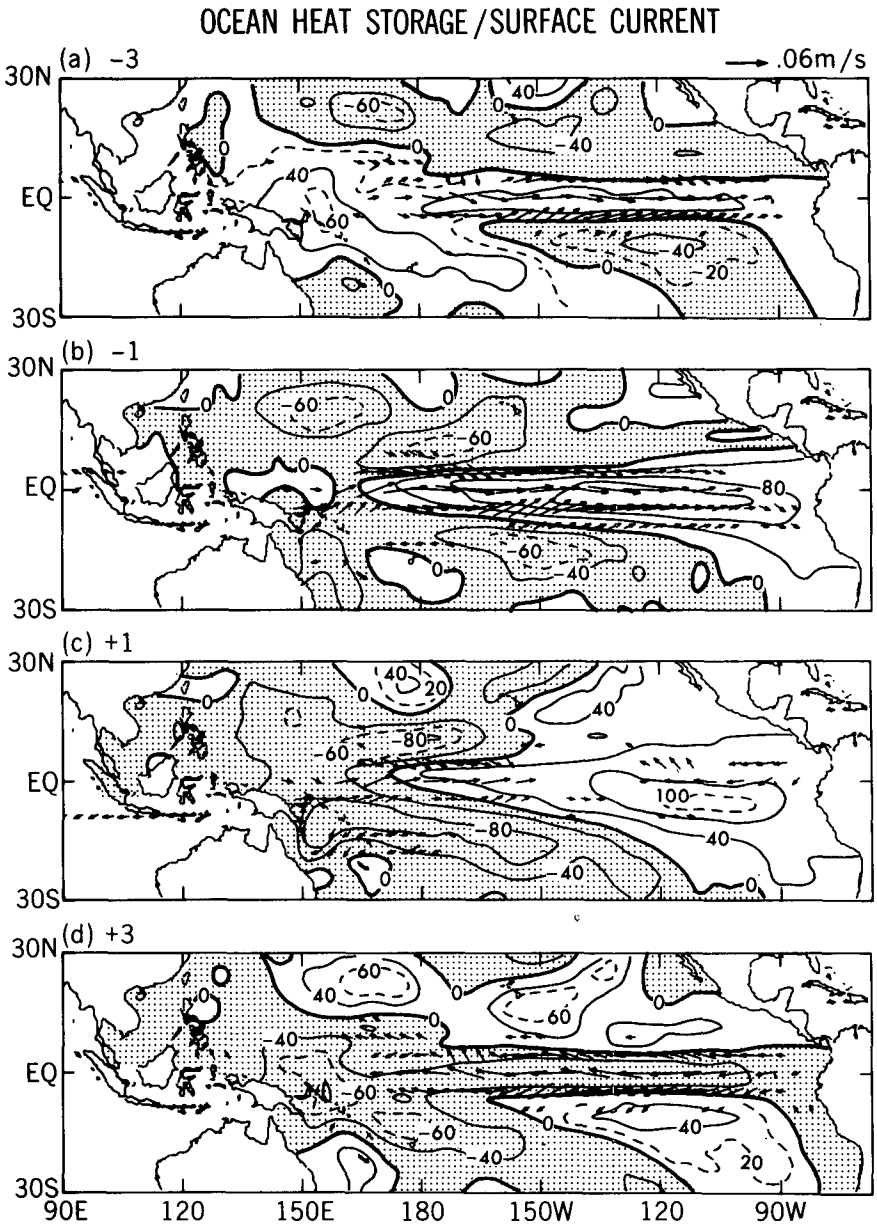

FIG. 14. As in Fig. 13, but for heat storage of the upper ocean (contours, interval: 40°C m) and horizontal velocity of the top ocean layer [arrows; see scale at the upper right corner of panel (a)]. Arrows too short to show up clearly have been omitted.

13–14 therefore depict the typical magnitudes of model anomalies associated with a 1°C warming or cooling event in the central Pacific.

The regression patterns for sea level pressure and surface wind stress in Fig. 13 indicate that the advent of a typical warm SST event [panels (a) and (b)] is coincident with weakening of the anticyclone over the eastern South Pacific, the equatorial trough over Indonesia, and the equatorial easterly trades. The wind stress pattern during the mature phase of the warm episode (Fig. 13c) is characterized by predominately southward-directed anomalies across the equator, as well as enhanced cyclonic surface circulation near the date line over the South Pacific. These features bear some resemblance to the observational results presented by Rasmusson and Carpenter (1982, Fig. 21) for the mature stage of ENSO. However, the simulated wind stress anomalies over the eastern equatorial Pacific are larger than the observed values. As the warm SST episode terminates, the east–west pressure seesaw

begins to swing in the opposite direction, with rising pressures in the South Pacific and falling pressures farther west (Fig. 13d). This phase in the ENSO cycle is marked by the occurrence of easterly wind stress anomalies over much of the ocean basin.

In response to the westward-migrating wind stress forcing shown in Fig. 13, the anomaly in the ocean current also propagates steadily westward (see arrows in Figs. 14a–c). When the eastward flow anomaly arrives at the western Pacific (Fig. 14c), a westward flow anomaly appears in the eastern Pacific. The latter feature in turn travels westward until it dominates much of the ocean basin two seasons later (Fig. 14d). It is also apparent from Fig. 14 that eastward flow anomalies in the surface current are accompanied by meridional inflow toward the equator, which implies the occurrence of reduced equatorial upwelling, whereas westward flow anomalies correspond to meridional outflow, which implies enhanced upwelling. The distributions of ocean heat storage during the warm phase (contours in Fig. 14) are characterized by an increase in equatorial heat storage at practically all longitudes and a decrease of heat storage in the off-equatorial waters, especially near 10°N and 10°S. In Fig. 14a, this behavior is most prominent to the east of the date line. During the next 2–4 seasons, the intensification and westward migration of the westerly winds (Figs. 13b–c) cause a further increase of the equatorial heat storage at most longitudes, at the expense of the heat storage in off-equatorial regions and in the far western equatorial Pacific (Figs. 14b–c). Next, easterly winds appear in the east and cause a decrease of the equatorial heat storage locally, as well as an increase of heat storage to the north and south. Once easterly winds prevail at most longitudes (Fig. 13d), the heat storage decreases all along the equator, while it increases in slightly higher latitudes (Fig. 14d). Inspection of the heat storage distributions in Fig. 14 gives the impression of westward propagation in off-equatorial latitudes. It is also noteworthy that the regression pattern for the heat storage during the peak of the warm phase (Fig. 14b) bears a considerable resemblance to the anomaly chart for the same field during the outstanding warm episode of year 44 (Fig. 9e).

e. *Phase relationships among various atmospheric and oceanic fluctuations*

In order to examine in greater detail the temporal and spatial relationships between different ENSO-like features, the regression coefficients between $c_1(t)$ of the SST field (see definition in section 5b) and several selected model variables have been evaluated at different time lags. The variations of these regression values with time lag are presented in Fig. 15. The data fields displayed here include SST itself, sea level pressure (SLP), precipitation rate, zonal wind stress (τ_x), surface zonal ocean current (U), and a measure of the meridional divergence of the surface ocean current (ΔV). The computations are based on model data for 150°W near the equator, where the SST fluctuations attain maximum amplitudes (see Fig. 7). The temporal variation of the regression coefficients for the SST field itself is depicted in all three panels of Fig. 15 (see stippling), so as to serve as a common frame of reference for discussing the evolution of other model fields. While interpreting the results presented in Fig. 15, it is useful to bear in mind that, for the westward-propagating ENSO-like phenomena considered here, a *lead* in the temporal phase of a field x relative to another field y at a given location is equivalent to a *westward* displacement of the extrema in x relative to those in y at a given time. Conversely, a *lag* in the temporal phase implies an *eastward* shift in the spatial phase. Hence, temporal lags and spatial displacements may be used interchangeably in describing the phase relationships between different variables.

The regression curves in the left panel of Fig. 15 indicate that the peak of the warm event (light stippling) near zero time lag occurs in conjunction with a maximum in precipitation, and a minimum in SLP. Hence the anomalous east-to-west gradient in SLP is enhanced to the *west* of the warm SST anomaly. This configuration results in a temporal lead (or, equivalently, westward displacement) of the eastward anomaly in U and τ_x relative to the SST signal (see the middle panel). The almost in-phase relationship between the fluctuations in U and τ_x is suggestive of an near-equilibrium response of the surface oceanic circulation to the atmospheric driving on the ENSO time scale. The Ekman drift associated with the eastward anomaly in U is seen to be accompanied by meridional convergence (right panel). Inspection of regression curves for longitudes other than 150°W (not shown) reveals that westward phase shifts of U, τ_x, and meridional convergence relative to the SST anomaly prevail throughout the central Pacific between 120°W and the date line. There exists a considerable longitudinal dependence in the phase relationship between the fluctuations in the vertical velocity in the top ocean layer (not shown) and the SST anomaly. In the eastern Pacific between 90° and 135°W, the maximum downwelling anomaly exhibits a lead of 1–2 seasons (or, equivalently, westward displacement) relative to the positive SST signal.

6. Heat budget of the top ocean layer

Regression patterns similar to those described in section 5d have been constructed using oceanic data for temperature and zonal current speed at depths ranging from 0 to 371 m. These results (not shown) indicate that the strongest thermal and circulation changes associated with ENSO occur in the topmost

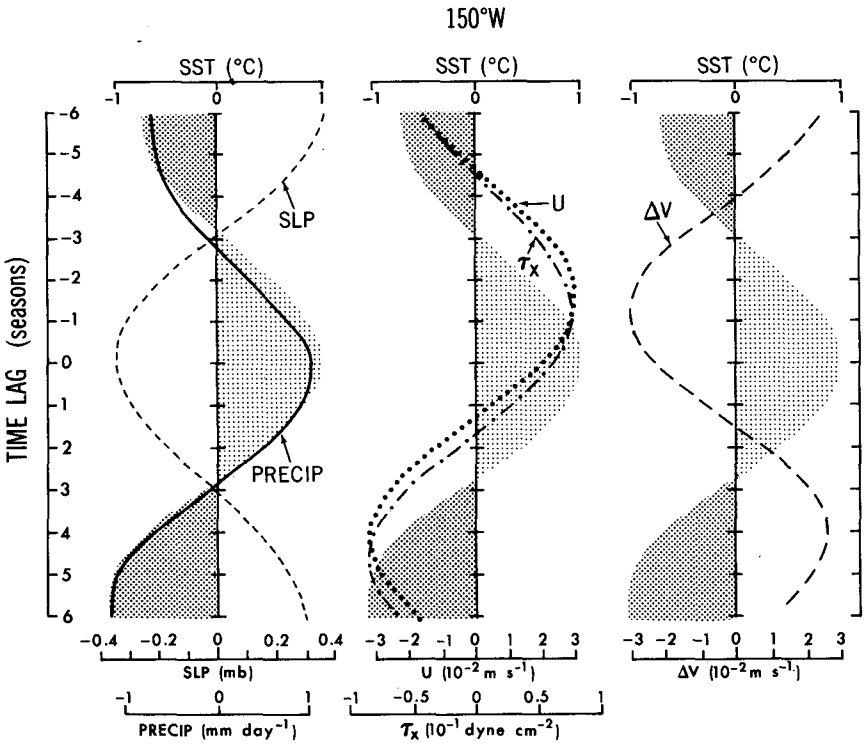

FIG. 15. Variations with time lag of the linear regression coefficients between $c_1(t)$ of the SST field and sea level pressure SLP and precipitation rate (left panel), zonal wind stress τ_x and zonal current speed U (middle panel), and meridional divergence ΔV (right panel). The corresponding regression coefficients for the SST data are depicted using stippling and are displayed in all three panels. Light and dense stippling indicate the warm and cold phases of the ENSO cycle, respectively. Results for SST, SLP, precipitation rate and τ_x are based on averages over 2.25°S and 2.25°N at 150°W. Results for U are based on averages over the gridpoint values at 4.5°S, 0°, and 4.5°N and at 150°W. Here ΔV has been computed by subtracting the meridional current at 4.5°S, 150°W from the corresponding quantity at 4.5°N, 150°W.

oceanic layer with a thickness of 51 m. Our attention will henceforth be focused on the role of various mechanisms in maintaining the heat balance of this particular layer.

a. The time-mean budget

The time-averaged equation for the temperature T of the surface ocean layer may be written as

$$\frac{\partial \bar{T}}{\partial t} = 0 = -\bar{u}\frac{\partial \bar{T}}{\partial x} - \bar{v}\frac{\partial \bar{T}}{\partial y} - \bar{w}\frac{\partial \bar{T}}{\partial z} + \bar{Q} + \overline{D_H} + \overline{D_V} + \bar{R}, \quad (1)$$

where the overbar denotes the time-averaging operator; u, v, w are the ocean current velocity components in the x, y, z directions, respectively; Q represents the heat gained from the atmosphere through the air–sea interface; and D_H and D_V are contributions from diffusive processes in the horizontal and vertical directions, respectively. The residual term R includes the effects of the convergence of heat transports by fluctuations from the time mean, as well as numerical inaccuracies in estimating various terms in the budget.

The relative importance of temperature advection by the time-mean flow [i.e., the first three terms on the right-hand side of Eq. (1)] in the local heat balance along the equator is essentially determined by the longitudinal variations of the climatologically averaged velocity and temperature gradient fields. The westward current speed is characterized by a broad maximum in the central Pacific, with much weaker zonal flows near the eastern and western boundaries (see Figs. 2b and 3b). The zonal temperature gradient along the equator is strongest between 160°E and 130°W (see Fig. 2a). Hence, one would expect the maximum zonal temperature advection to take place in the central Pacific. The intensity of the meridional outflow (Fig. 2b) is rather uniform between 180° and 130°W, and drops off sharply near the South American coast. The meridional temperature gradient in the deep tropics (Fig. 2a) is strongest between 160° and 100°W. The merid-

ional temperature advection term would therefore also attain maximum amplitudes in the central portion of the basin. The largest values in both upwelling and vertical stratification (see Fig. 3a) are located in the eastern Pacific, thus leading to an extremum in vertical temperature advection in that region.

The longitudinal variations of every term in the time-averaged equatorial heat budget [Eq. (1)] are summarized in Fig. 16. The spatial derivatives in all terms were evaluated by finite-difference schemes that follow as closely as possible the numerics actually used in the ocean model. The results shown here are based on averages over the computations at grid points lying between 6.75°S and 6.75°N. A five-point running mean smoother in the longitudinal direction has been applied to the individual terms. The terms Q and D_H are positive throughout the domain of interest, and are hence displayed above the zero line in a cumulative fashion. The three advection terms as well as D_V are negative and are shown below the zero line, again in a cumulative format. The term R, obtained as a residual from the six remaining terms on the right-hand side of Eq. (1), is displayed at the bottom of Fig. 16 with the same scale. The small magnitude of R at all longitudes indicates that a near balance is achieved among temperature advection by the time-mean flow, diffusion, and diabatic heating and that contributions from the covariance between subseasonal velocity and temperature perturbations and from numerical inaccuracies are negligible.

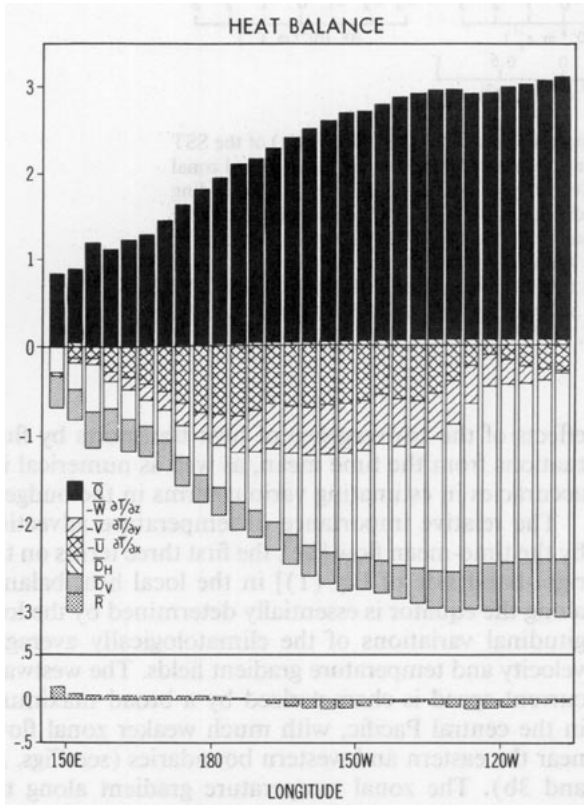

FIG. 16. Longitudinal variations along the equator of the cumulative contributions of various processes to the climatological heat balance of the top ocean layer. The positive contributions of $\bar{Q}$ and $\bar{D}_H$ are presented above the zero line. The negative heat advection terms and $\bar{D}_V$ are shown below the zero line. The residual is plotted separately at the bottom of the diagram. The results shown here are based on averages over the 6.75°S–6.75°N zone. A five-point running mean smoother in the longitudinal direction has been applied to the individual budget terms.

The zonal dependence of the three advection terms is consistent with the earlier discussion on the spatial variability of the time-mean current velocity and temperature gradients. Near the date line, cold advection due to the westward current is slightly stronger than the effects of upwelling and meridional outflow of cold equatorial waters. Between 160° and 110°W, the zonal and meridional advection terms have similar magnitudes, but both terms are weaker than the upwelling effect. In the far eastern Pacific, the advective process is dominated by upwelling of cold water.

Effects of diffusive processes in the horizontal direction are seen to be relatively small. Vertical diffusion is substantially stronger, and its contribution to the heat budget increases from west to east. This longitudinal variation of D_V is related to the strengthening vertical temperature stratification from west to east (Fig. 3a). The negative contributions of temperature advection and vertical diffusion are counterbalanced by heat input Q from the overlying atmosphere. The latter source term increases almost monotonically from the western Pacific to the South American coast.

b. *The budget for ENSO-like anomalies*

The equation for temperature perturbations in the surface ocean layer may be written as

$$\frac{\partial T'}{\partial t} = -\bar{u}\frac{\partial T'}{\partial x} - u'\frac{\partial \bar{T}}{\partial x} - u'\frac{\partial T'}{\partial x} - \bar{v}\frac{\partial T'}{\partial y} - v'\frac{\partial \bar{T}}{\partial y} - v'\frac{\partial T'}{\partial y} - \bar{w}\frac{\partial T'}{\partial z} - w'\frac{\partial \bar{T}}{\partial z} - w'\frac{\partial T'}{\partial z} + Q' + D'_H + D'_V + R', \quad (2)$$

where the primes denote deviations from time averages. In computing the various terms in Eq. (2), $\bar{x}$ is taken to be the climatological average of x, whereas x' is taken to be the regression coefficient of x versus the temporal coefficients of the leading EEOF of the SST field (see results in section 5d). In effect, the substitution scheme adopted here equates the linear terms of the heat balance to the regression coefficients of the corresponding terms versus $c_1(t)$ of the SST field. By substituting the regression values corresponding to different time lags between the model fields and $c_1(t)$, the temporal evo-

lution of the heat balance through the ENSO-like cycle may be investigated. The present method hence offers a convenient procedure for estimating the individual heat budget terms in various stages of the simulated ENSO events corresponding to a 1°C SST anomaly in the central equatorial Pacific. As was done in the time-mean budget, all spatial and temporal derivatives in Eq. (2) were estimated by finite-difference schemes consistent with the model numerics.

In Fig. 17 are shown the distributions of the regression coefficients for the linear advection terms in Eq. (2) as functions of longitude and time lag. The values shown here have been obtained by averaging over the grid points lying between 6.75°S and 6.75°N. The nonlinear terms $u'\partial T'/\partial x$, $v'\partial T'/\partial y$, and $w'\partial T'/\partial z$ are typically weaker than the corresponding linear terms by a factor of 5–10 and are therefore not presented here. By recalling the results in Fig. 11, we note here that zero time lag coincides with the positive peak of the SST anomaly over the equatorial Pacific, whereas time lags of ±6 seasons correspond to minimum SST in the same region. The panels in Fig. 17 indicate that, whereas westward-propagating signals are apparent in most of the terms shown here, the contributions of individual advective processes to the heat balance exhibit considerable variability in space and time. The following phenomena are particularly noteworthy.

- At 2–4 seasons prior to the occurrence of the maximum SST anomaly, the heat budget is dominated by anomalous meridional inflow of warm water toward the equator ($-v'\partial\bar{T}/\partial y$) near 120°W (see Figs. 17c and 14a) and by anomalous downwelling ($-w'\partial\bar{T}/\partial y$) near the South American coast (Fig. 17e).
- The contributions to the heat balance due to anomalous eastward advection from the climatologically warm region in the western Pacific toward the central portion of the basin ($-u'\partial\bar{T}/\partial x$, see Figs. 17a and 14b) and to $-v'\partial\bar{T}/\partial y$ near 150°W (Fig. 17c) are most significant at about one season before the mature warm phase.
- The peak of the warm SST anomaly at zero time lag coincides with strong advections of the positive temperature anomaly by the westward time-mean current ($-\bar{u}\partial T'/\partial x$, see Fig. 17b) west of the date line and by the climatological meridional outflow ($-\bar{v}\partial T'/\partial y$, see Fig. 17d) in the central Pacific.
- At about one season following the peak of the warm event, the eastern Pacific comes under the influences of cold temperature advection due to $-\bar{u}\partial T'/\partial x$ (Fig. 17b) and $-v'\partial\bar{T}/\partial y$ (Fig. 17c).
- The advent of the cold phase is accompanied by a sequence of advective processes similar to those described above, except for a sign reversal.
- The vertical advection of the temperature anomaly by the time-mean flow $-\bar{w}\partial T'/\partial z$ (Fig. 17f) is seen to make only minor contributions to the heat balance throughout the ENSO cycle. It is, however, worth noting that this term is crucially dependent on vertical resolution of the ocean model. A model with a mixed layer better resolved than that in the LR model could conceivably simulate a very different vertical profile of T' and thereby yield considerably larger magnitudes for $-\bar{w}\partial T'/\partial z$.

The results shown in Fig. 17 suggest that the spatial dependence of the relative magnitudes of various advective terms in the perturbation heat balance is similar to that in the time-mean balance (see section 6a). In particular, we note the prominence of $-w'\partial\bar{T}/\partial z$ east of 120°W due to the enhanced climatological vertical temperature stratification $\partial\bar{T}/\partial z$ in that region (Fig. 3a), whereas $-u'\partial\bar{T}/\partial x$, $-v'\partial\bar{T}/\partial y$, and $-\bar{v}\partial T'/\partial y$ make comparable contributions between the date line and 120°W, and $-\bar{u}\partial T'/\partial x$ is the dominant term west of the date line.

The important terms of the heat budget for T' [Eq. (2)] are displayed in Fig. 18. The diffusion terms D'_H and D'_V (not shown) are typically weaker than the terms in Fig. 18 by factors of 10–20 and 3–5, respectively. The characteristic shape of the pattern for the temperature tendency $\partial T'/\partial t$ in panel (a) is again suggestive of westward-migrating SST anomalies. The values in panel (b) represent the sum of the contributions from all the advective terms (i.e., the six components in Fig. 17 plus the much smaller nonlinear terms). The pattern in that panel also illustrates the westward spread with time of the influences of the net temperature advection. The strongest anomalous heat fluxes across the air–sea interface takes place within the 150°W–180° zone [panel (c)], where the SST perturbations attain largest amplitudes (see Fig. 7). The strong, negative temporal correlation between Q' (Fig. 18c) and T' (Fig. 12a) between 150°W and the date line implies that the diabatic heat fluxes essentially act as a damping mechanism in those longitudes. The time scale associated with this dissipative effect, as estimated by T'/Q', is approximately 500 d. Since the corresponding time scale for the growth and decay of the SST anomalies themselves, as given by

$$T' \Big/ \frac{\partial T'}{\partial t},$$

is only about 200 days (see Figs. 15 and 18a), the dissipation due to Q' may be viewed as a minor, but by no means negligible, component of the surface heat budget. Comparison among the first three panels of Fig. 18 indicates that, in the eastern Pacific, temperature advection in both horizontal and vertical directions is the major contributor to the local $\partial T'/\partial t$, whereas in the vicinity of the date line, the advective processes are offset by both $\partial T'/\partial t$ and heat exchange with the atmosphere.

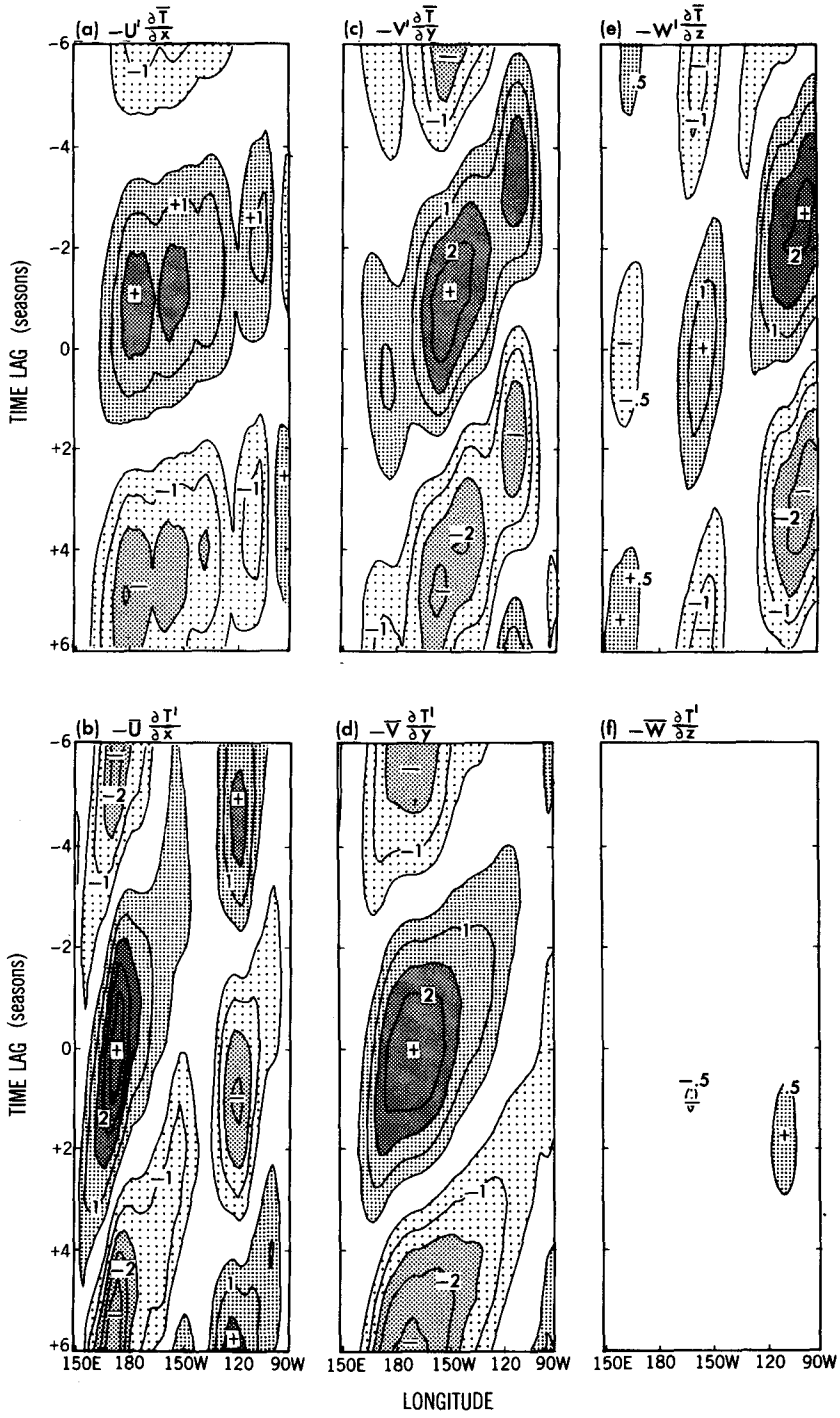

FIG. 17. Longitude–time lag distributions of the linear regression coefficients between $c_1(t)$ of the SST field and the gridpoint values of (a) $-u'\partial\bar{T}/\partial x$, (b) $-\bar{u}\partial T'/\partial x$, (c) $-v'\partial\bar{T}/\partial y$, (d) $-\bar{v}\partial T'/\partial y$, (e) $-w'\partial\bar{T}/\partial z$, and (f) $-\bar{w}\partial T'/\partial z$ (contour interval: 5×10^{-9} °C s^{-1}). The results shown here are based on averages over the 6.75°S–6.75°N zone. The zero contour has been omitted for sake of clarity. Negative (positive) time lags indicate gridpoint data leading (lagging) $c_1(t)$. A five-point running mean smoother in the longitudinal direction has been applied to the individual budget terms.

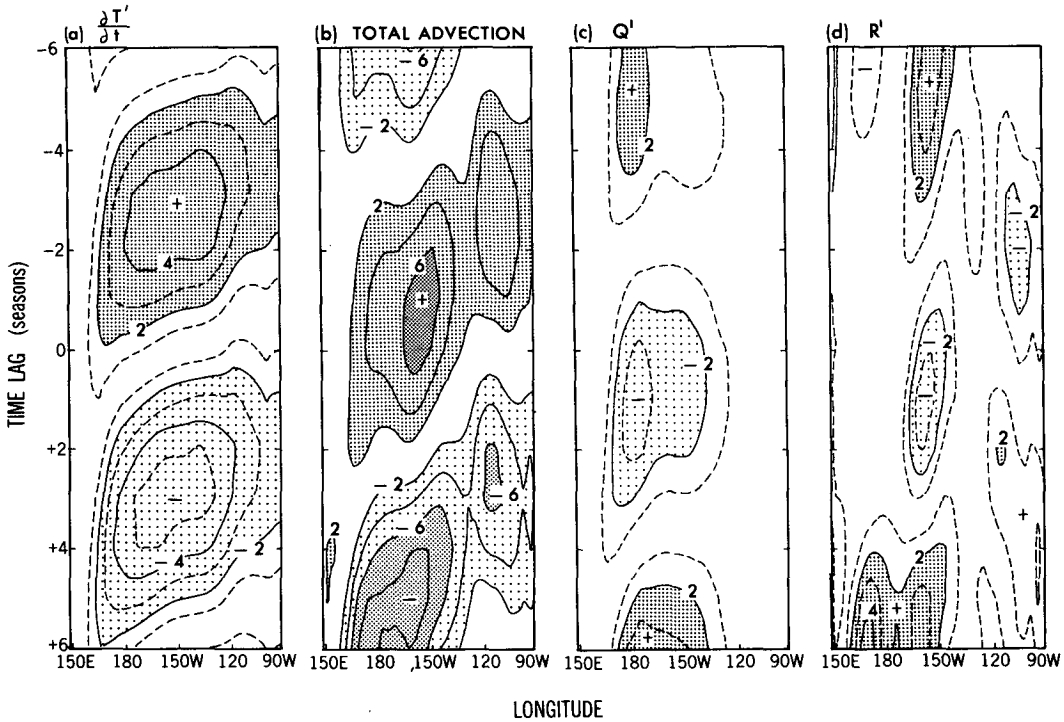

FIG. 18. As in Fig. 17, but for (a) $\partial T'/\partial t$ and (b) sum of the nine advective terms in Eq. (2), (c) Q', and (d) R'. Interval between solid contours: 2×10^{-8} °C s^{-1}.

The term R', which was obtained as a residual of all known terms (including D'_H and D'_V) in Eq. (2), is shown in panel (d). Contributors to this term include numerical inaccuracies of the finite-difference schemes, effects of high-frequency transients with time scales shorter than the 3-month averages used in the present analysis, as well as approximations made in using the regression coefficients to estimate various primed quantities in Eq. (2). The pattern of R' is notably less organized than those in the other panels of Fig. 18. The magnitudes of the isolated extrema in this term are typically smaller than the net advective and tendency terms [panels (b) and (a)] by factors of 3–4 and 2–2.5, respectively. Hence, a near balance among the tendency, advection, and heat flux terms is achieved in most phases of the ENSO-like cycle and at most longitudes.

7. Summary and discussion

The evidence presented in this study indicates that, notwithstanding several obvious deficiencies in the climatology of the ocean model due to insufficient resolution (e.g., the absence of the North Equatorial Countercurrent, the weak Equatorial Undercurrent, and the rather crude mixed-layer structure, see Figs. 2–4), the coupled system is capable of generating recurrent modes of variability with interannual time scales (Figs. 5–7). The most prevalent mode is associated with a family of interrelated meteorological and oceanographic phenomena that bear some qualitative resemblance to the warm and cold phases of observed ENSO cycles (Figs. 8–10). However, the amplitude of the simulated events is considerably weaker than the observed values, and the model signals near the South American coasts and the western end of the Pacific basin are generally less distinct than those detected in the central Pacific. The typical space–time evolution of the ENSO-like episodes appearing in the model is characterized by a systematic westward propagation of SST, zonal wind stress, and zonal surface current anomalies along the equator (Figs. 11–14). The zonal scale of these anomalies is somewhat smaller than the width of the Pacific basin, so that when perturbations of a given polarity arrive at the western Pacific, perturbations of the opposite polarity emerge off the Peru–Ecuador coast and likewise migrate westward.

Figure 15 provides a concise summary of the phase relationships among various atmospheric and oceanic fluctuations over the central equatorial Pacific during a typical ENSO-like cycle appearing in the LR integration. Particularly noteworthy is the westward displacement of the zonal wind stress anomalies with respect to the SST anomalies at 150°W (see middle panel of Fig. 15). As a result of this longitudinal phase shift, the strongest positive zonal advection of the time-mean

temperature field ($-u'\partial\bar{T}/\partial x$), as well as the strongest meridional inflow of warmer off-equatorial waters ($-v'\partial\bar{T}/\partial y$), occurs *west* of the warm SST anomaly. Hence, these processes contribute to the continued westward migration of the SST anomaly. The strong contributions of the two advection terms considered here are illustrated by the heat budget analysis of the surface ocean (Figs. 17a and 17c). By the same token, the western displacement of the downwelling signal relative to the warm SST anomaly in the eastern Pacific (not shown, refer to the discussion at the end of section 5e) is also conducive to westward propagation of the ENSO-like features. The space–time evolution of the term $-w'\partial\bar{T}/\partial z$ in Fig. 17e clearly indicates the importance of the vertical motion field in initiating the warm and cold events off the South American coast. The time-mean westward current also acts to push the SST perturbations westward, especially at 120°W and near the date line (see the pattern for $-\bar{u}\partial T'/\partial x$ in Fig. 17b). The anomaly patterns for ocean heat storage (Fig. 14) suggest that substantial meridional heat exchange occurs between the equatorial and off-equatorial waters in the course of the simulated ENSO episodes. The importance of the advective processes in the meridional direction ($-v'\partial\bar{T}/\partial y$ and $-\bar{v}\partial T'/\partial y$) is confirmed by the heat budget study (Figs. 17c and 17d).

In consonance with the model features described here, Meehl (1990) has reported that the NCAR coarse-grid coupled GCM also produces westward-migrating SST anomalies in the central equatorial Pacific, with amplitudes that are weaker than observed. The westward displacement of the westerly wind stress and suppressed upwelling signals relative to the warm SST anomaly are also discernible in the NCAR simulation.

The recent stability analysis of coupled ocean–atmosphere modes by Neelin (1991) is relevant to the Southern Oscillation simulated in the present model. He considered a system in which the atmosphere is at all times in equilibrium with the SST patterns and in which the ocean is in dynamical equilibrium with the surface winds. The in-phase relationship between zonal wind stress and zonal oceanic current, as illustrated in the middle panel of Fig. 15, is indicative of such an equilibrium response in the LR model. Hence, the only explicit time dependence in the equations of motion used by Neelin appears in the sea surface temperature equation, and the stability analysis is greatly simplified. By considering a heat budget analogous to that depicted in Fig. 17, Neelin (1991) found westward-traveling coupled ocean–atmosphere modes similar to those described in this paper. The differences between the coupled mode described here and the coupled modes excited in other models will be discussed in greater detail in Philander et al. (1992).

The model run examined here has been conducted using constant annual mean insolation. It is, however, known from various observational studies that the seasonal cycle exerts a considerable influence on the timing of the occurrence of ENSO, as well as on the degree of interaction between the tropics and extratropics during ENSO (e.g., Horel and Wallace 1981; Rasmusson and Carpenter 1982). The extent to which these seasonal modulations of ENSO can be mimicked by coupled GCMs remains to be ascertained by diagnosing simulations incorporating the seasonal cycle.

Since a majority of the observational ENSO studies are concerned with meteorological and oceanographic features in the Pacific, and since almost all of the modeling investigations (including the HR integration) conducted to date are aimed at reproducing the ENSO signals in that basin, we have restricted the present model analysis to the interannual variability in the tropical Pacific only. Bearing in mind that the LR experiment is a global simulation with the atmosphere interacting with all parts of the World Ocean, it would be of interest to examine the nature of the fluctuations occurring over the Atlantic and Indian oceans as well. Another topic worth pursuing is the interaction between ENSO-like phenomena in the Pacific and the prevalent modes residing in the other basins, and between the interannual variations occurring in the tropics and in the higher latitudes. The available observational evidence (e.g., Horel and Wallace 1981) indicates a considerable seasonal dependence in the influence of ENSO events on the extratropical atmospheric circulation. Hence, the nature of tropical–extratropical interactions accompanying ENSO episodes should preferably be investigated on the basis of model runs with seasonally varying insolation.

It is evident from the budget computations in section 6 that the equatorial heat balance for the surface ocean in the low-resolution coupled model is mainly governed by linear advective processes, whereas nonlinear contributions from ocean eddies and from perturbations with subseasonal time scales play a relatively minor role. The latter result could partially be attributed to the suppression of various equatorial ocean wave modes as a result of inadequate model resolution in the LR version. Data generated by the high-resolution model, with its more realistic climatology and its more accurate representation of equatorial ocean waves, have been analyzed so as to delineate the similarities and differences among the ENSO-like features appearing in the two coupled systems, and to assess the impact of ocean wave dynamics on ENSO. These results will be presented in the following companion paper by Philander et al. (1992).

Acknowledgments. We are indebted to S. Manabe and R. J. Stouffer for their generosity and cooperation in making available to us the data archives of their LR integration. We have benefited from many helpful discussions on various ENSO topics with I. M. Held, who has also examined an earlier draft of this manuscript

and offered suggestions for improving the presentation of results. T. P. Barnett, K. P. Hamilton, A. C. Hirst, A. H. Oort, and the official reviewers have also made several constructive comments on this paper. The figures were prepared by the Scientific Illustration Group at GFDL.

REFERENCES

Anderson, D. L. T., and J. P. McCreary, 1985: Slowly propagating disturbances in a coupled ocean–atmosphere model. *J. Atmos. Sci.*, **42**, 615–628.

Arkin, P. A., J. D. Kopman, and R. W. Reynolds, 1983: *1982–83 El Niño/Southern Oscillation Event Quick Look Atlas.* Climate Analysis Center/NOAA.

Battisti, D. S., 1988: The dynamics and thermodynamics of a warming event in a coupled tropical atmosphere–ocean model. *J. Atmos. Sci.*, **45**, 2889–2919.

——, and A. C. Hirst, 1989: Interannual variability in the tropical ocean–atmosphere system: Influence of the basic state, ocean geometry and nonlinearity. *J. Atmos. Sci.*, **46**, 1687–1712.

Bjerknes, J., 1969: Atmospheric teleconnections from the equatorial Pacific. *Mon. Wea. Rev.*, **97**, 163–172.

Bryan, K., and L. Lewis, 1979: A water mass model of the world ocean. *J. Geophys. Res.*, **84**, 2503–2517.

Bryden, H. L., and E. C. Brady, 1985: Diagnostic model of the three-dimensional circulation in the upper equatorial Pacific Ocean. *J. Phys. Oceanogr.*, **15**, 1255–1273.

Cane, M. A., and S. E. Zebiak, 1985: A theory for El Niño and the Southern Oscillation. *Science*, **228**, 1085–1087.

Colin, C., C. Henin, P. Hisard, and C. Oudot, 1971: Le Courant de Cromwell dans le Pacifique central en féverier. *Cah. ORSTOM, Ser. Oceanogr.*, **9**, 167–186.

Dorman, C. E., and R. H. Bourke, 1979: Precipitation over the Pacific Ocean, 30°S to 60°N. *Mon. Wea. Rev.*, **107**, 896–910.

——, and ——, 1981: Precipitation over the Atlantic Ocean, 30°S to 70°N. *Mon. Wea. Rev.*, **109**, 554–563.

Gordon, C., 1989: Tropical ocean–atmosphere interactions in a coupled model. *Phil. Trans. Roy. Soc. London*, **A329**, 207–223.

Hellerman, S., and M. Rosenstein, 1983: Normal monthly windstress over the world ocean with error estimates. *J. Phys. Oceanogr.*, **13**, 1093–1104.

Hirst, A. C., 1986: Unstable and damped equatorial modes in simple coupled ocean–atmosphere models. *J. Atmos. Sci.*, **43**, 606–630.

Horel, J. D., 1982: On the annual cycle of the tropical Pacific atmosphere and ocean. *Mon. Wea. Rev.*, **109**, 1863–1878.

——, and J. M. Wallace, 1981: Planetary-scale atmospheric phenomena associated with the Southern Oscillation. *Mon. Wea. Rev.*, **109**, 813–829.

Hsu, C-P. F., and J. M. Wallace, 1976: The global distribution of annual and semiannual cycles in sea level pressure. *Mon. Wea. Rev.*, **104**, 1597–1601.

Jaeger, L., 1976: Monthly precipitation maps for the entire earth (in German). *Ber. Dtsch. Wetterdienstes*, **18**, 38 pp.

Knauss, J. A., 1978: *Introduction to Physical Oceanography.* Prentice Hall, 338 pp. [ISBN 0-13-493015-0]

Latif, M., J. Biercamp and H. von Storch, 1988: The response of a coupled ocean–atmosphere model to wind bursts. *J. Atmos. Sci.*, **45**, 964–979.

Lau, K. M., and P. H. Chan, 1985: Aspects of the 40–50-day oscillation during the northern winter as inferred from outgoing longwave radiation. *Mon. Wea. Rev.*, **113**, 1889–1909.

Lau, N-C., 1985: Modeling the seasonal dependence of the atmospheric response to observed El Niños in 1962–76. *Mon. Wea. Rev.*, **113**, 1970–1996.

Manabe, S., and D. G. Hahn, 1981: Simulation of atmospheric variability. *Mon. Wea. Rev.*, **109**, 2260–2286.

——, and R. J. Stouffer, 1988: Two stable equilibrium of a coupled ocean–atmosphere model. *J. Climate*, **1**, 841–866.

Meehl, G. A., 1990: Seasonal cycle forcing of El Niño–Southern Oscillation in a global, coupled ocean–atmosphere GCM. *J. Climate*, **3**, 72–98.

Nakamura, H., M. Tanaka, and J. M. Wallace, 1987: Horizontal structure and energetics of Northern Hemisphere wintertime teleconnection patterns. *J. Atmos. Sci.*, **44**, 3377–3391.

Neelin, J. D., 1989: Interannual oscillations in an ocean general circulation model coupled to a simple atmosphere model. *Phil. Trans. Roy. Soc. London*, **A329**, 180–205.

——, 1990: A hybrid coupled general circulation model for El Niño studies. *J. Atmos. Sci.*, **47**, 674–693.

——, 1991: The slow sea surface temperature mode and the fast-wave limit: Analytic theory for tropical interannual oscillations and experiments in a hybrid coupled model. *J. Atmos. Sci.*, **48**, 584–606.

——, M. Latif, M. A. F. Allaart, M. A. Cane, U. Cubasch, W. L. Gates, P. R. Gent, M. Ghil, C. Gordon, N-C. Lau, C. R. Mechoso, G. A. Meehl, J. M. Oberhuber, S. G. H. Philander, P. S. Schopt, K. R. Sperber, A. Sterl, T. Tokioka, J. Tribbia, and S. E. Zebiak, 1992: Tropical air–sea interaction in general circulation models. *Climate Dyn.*, **7**, in press.

Philander, S. G. H., and A. D. Siegel, 1985: Simulation of El Niño of 1982–83. *Coupled Ocean–Atmosphere Models.* J. Nihoul, Ed., Elsevier, 517–541.

——, and W. J. Hurlin, 1988: The heat budget of the tropical Pacific Ocean in a simulation of El Niño of 1982–1983. *J. Phys. Oceanogr.*, **8**, 926–931.

——, R. C. Pacanowski, N-C. Lau, and M. J. Nath, 1992: Simulation of ENSO with a global atmospheric GCM coupled to a high-resolution, tropical Pacific ocean GCM. *J. Climate*, **5**, 308–329.

Ramage, C. S., C. W. Adams, A. M. Hori, B. J. Kilonsky, and J. C. Sadler, 1980: Meteorological atlas of the 1972–73 El Niño. UHMET, 80-03, Dept. Meteorology, University of Hawaii, Honolulu, 101 pp.

Rasmusson, E. M., and T. H. Carpenter, 1982: Variations in tropical sea surface temperature and surface wind fields associated with the Southern Oscillation/El Niño. *Mon. Wea. Rev.*, **110**, 354–384.

——, and J. M. Wallace, 1983: Meteorological aspects of the El Niño/Southern Oscillation. *Science*, **222**, 1195–1202.

Schopf, P. S., and M. J. Suarez, 1988: Vacillations in a coupled ocean–atmosphere model. *J. Atmos. Sci.*, **45**, 549–566.

Weare, B. C., and J. S. Nasstrom, 1982: Examples of extended empirical orthogonal function analyses. *Mon. Wea. Rev.*, **110**, 481–485.

Zebiak, S. E., and M. A. Cane, 1987: A model ENSO. *Mon. Wea. Rev.*, **115**, 2262–2278.